ELEMENTA
Science of the Anthropocene

Light, B, et al. 2022. Arctic sea ice albedo:. *Elem Sci Anth*, 10: 1.
DOI: https://doi.org/10.1525/elementa.2021.000103

RESEARCH ARTICLE

Arctic sea ice albedo: Spectral composition, spatial heterogeneity, and temporal evolution observed during the MOSAiC drift

Bonnie Light[1,*], Madison M. Smith[1], Donald K. Perovich[2], Melinda A. Webster[3], Marika M. Holland[4], Felix Linhardt[5], Ian A. Raphael[2], David Clemens-Sewall[2], Amy R. Macfarlane[6], Philipp Anhaus[7], and David A. Bailey[4]

The magnitude, spectral composition, and variability of the Arctic sea ice surface albedo are key to understanding and numerically simulating Earth's shortwave energy budget. Spectral and broadband albedos of Arctic sea ice were spatially and temporally sampled by on-ice observers along individual survey lines throughout the sunlit season (April–September, 2020) during the Multidisciplinary drifting Observatory for the Study of Arctic Climate (MOSAiC) expedition. The seasonal evolution of albedo for the MOSAiC year was constructed from spatially averaged broadband albedo values for each line. Specific locations were identified as representative of individual ice surface types, including accumulated dry snow, melting snow, bare and melting ice, melting and refreezing ponded ice, and sediment-laden ice. The area-averaged seasonal progression of total albedo recorded during MOSAiC showed remarkable similarity to that recorded 22 years prior on multiyear sea ice during the Surface Heat Budget of the Arctic Ocean (SHEBA) expedition. In accord with these and other previous field efforts, the spectral albedo of relatively thick, snow-free, melting sea ice shows invariance across location, decade, and ice type. In particular, the albedo of snow-free, melting seasonal ice was indistinguishable from that of snow-free, melting second-year ice, suggesting that the highly scattering surface layer that forms on sea ice during the summer is robust and stabilizing. In contrast, the albedo of ponded ice was observed to be highly variable at visible wavelengths. Notable temporal changes in albedo were documented during melt and freeze onset, formation and deepening of melt ponds, and during melt evolution of sediment-laden ice. While model simulations show considerable agreement with the observed seasonal albedo progression, disparities suggest the need to improve how the albedo of both ponded ice and thin, melting ice are simulated.

Keywords: Sea ice, Albedo, Melt ponds, Ice-optics, Sediment, Surface scattering layer

1. Introduction

The Arctic sea ice cover plays a prominent role as both indicator and amplifier of global climate change, in large part because of its vast area, modest thickness, and high albedo. These properties result in an ice-albedo feedback mechanism (Hall, 2004; Thackeray and Hall, 2019; Wunderling et al., 2020), whereby changes in ice concentration or changes in the albedo of the ice cover drive potentially amplifying changes in the surface heat budget. The albedo depends strongly on snow depth and properties (Flanner and Zender, 2006; Aoki et al., 2011), the optical characteristics of bare, melting sea ice (Perovich et al., 2002), and the formation, extent, and development of surface melt ponds (Polashenski et al., 2012; Webster et al., 2015; Polashenski et al., 2017). While these factors are essential for understanding the state of the ice cover, they also determine the albedo of the ice cover and the strength of the ice-albedo feedback.

At the onset of the sunlit season, sea ice is largely covered by snow and its albedo is relatively high and spatially homogeneous. In summer, however, changes in the optical properties of the ice cover result in decreased magnitude of the albedo along with increased temporal

[1] Polar Science Center, Applied Physics Laboratory, University of Washington, Seattle, WA, USA
[2] Thayer School of Engineering, Dartmouth College, Hanover, NH, USA
[3] Geophysical Institute, University of Alaska Fairbanks, Fairbanks, AK, USA
[4] National Center for Atmospheric Research, Boulder, CO, USA
[5] Christian-Albrechts-Universität zu Kiel, Institut für Geographie, Kiel, Germany
[6] WSL Institute for Snow and Avalanche Research SLF, Davos, Switzerland
[7] Alfred-Wegener-Institut, Helmholtz-Zentrum für Polar- und Meeresforschung, Bremerhaven, Germany

* Corresponding author:
Email: bonlight@uw.edu

and spatial variability (Perovich et al., 2002). Significant changes occur on sub-weekly time scales, and melt ponds introduce sharp contrasts on sub-meter spatial scales. As a result, albedo measurements with a footprint larger than about 5 m, such as those measured from drone, helicopter, or satellite, rarely represent individual surface types in physically meaningful ways. Albedo measurements taken by surface observers provide a detailed, time-resolved record of specific surface conditions and ice types (e.g., Langleben, 1969; 1971; Grenfell and Maykut, 1977; Grenfell and Perovich, 1984; Perovich, 1991; 1994; Hanesiak et al., 2001; Perovich et al., 2002; Ehn et al., 2006; Nicolaus et al., 2010; Perovich and Polashenski, 2012; Light et al., 2015; Xia et al., 2015; Zhu et al., 2021). Albedo measurements are most informative when coordinated with detailed physical property observations, including surface type description, snow and ice thickness, snow grain size and density, ice freeboard, temperature, and texture, and melt pond properties.

Both the spectral (α_λ) and broadband (α_{tot}; "total" or wavelength-integrated) albedo provide useful insight into the characteristics of the sea ice cover and its partitioning of solar radiation. The development of "structural-optical" models (e.g., Light et al., 2004) that resolve variations in the physical and optical properties of the ice depend on extensive knowledge of α_λ for a variety of ice types and conditions. Because ice and liquid water absorb blue light (λ approximately 300–500 nm) very weakly, α_λ at these wavelengths is determined by light scattering due to inclusions of brine and gas and can be modified by light absorption due to even small concentrations of impurities (e.g., soot, sediment) and biological constituents. Because the absorption of pure ice increases with wavelength, α_λ at red (λ approximately 650–700 nm) and near-infrared wavelengths (λ approximately 700–2500 nm) is determined increasingly by the properties of the uppermost portions of the ice cover. Analogously, measurements of the total albedo are needed to assess energy budgets and inform ice mass budget studies. For these reasons, independent, but co-located and simultaneous, observations of α_{tot} and α_λ are especially informative.

As large-scale modeling shows that the physical state of the Arctic sea ice cover has strong sensitivity to ice albedo (Holland and Landrum, 2015) and the summer albedo shows strong sensitivity to short time-scale changes in ice properties (Perovich et al., 2002), the albedo is a common target for model tuning (Kay et al., 2022). However, as the area-averaged albedo is an integration across a variety of surface types, albedo tuning is sometimes done in a manner inconsistent with surface properties. For example, the same change to area-averaged albedo on ponded ice could result from increased pond fraction or decreased pond albedo. Ideally, models predict the surface state and compute the area-averaged albedo based on the area fraction of each surface type and their optical properties. Many of the CMIP6-era coupled climate models (Keen et al., 2021), such as the Community Earth System Model (CESM2), use a radiative transfer model (Briegleb and Light, 2007; Holland et al., 2012) to calculate the surface albedo for multiple surface-cover classes within each ice thickness category. These surface cover categories include snow-covered sea ice, bare ice, and melt ponds, and the use of five ice-thickness categories is common. Development and validation of such models rely on accurate albedo observations of individual surface types coordinated with detailed physical property observations.

Knowledge of the albedo of individual surface types is fundamental to the characterization of a heterogeneous sea ice surface. The highest albedos result from cold, dry snow accumulated on the ice. As the snow metamorphoses and eventually begins to melt, the albedo quickly drops, first in response to grain coarsening within the snow, then to the presence of liquid water within the snow and the formation of areas with ponded liquid water. At the height of summer, the ice cover can typically be described as a mixture of bare (snow-free), melting ice (sometimes referred to as "white ice") and ponded ice. As freezing conditions return at the end of summer and into the autumn, pond surfaces freeze and snow once again accumulates on the ice cover.

Over the decades, observational campaigns have characterized the evolution of sea ice albedo. Some of these studies have focused on landfast ice (e.g., Langleben, 1969; Grenfell and Perovich, 1984; Perovich, 1994; Hanesiak et al., 2001; Grenfell and Perovich, 2004; Ehn et al., 2006; Perovich and Polashenski, 2012; Zhu et al., 2021). While such studies are logistically tractable, they lack generality due to differences in landfast ice characteristics and are frequently affected by terrestrial influences on the heat budget and the introduction of terrigenous material. Observations of the temporal changes in albedo on drifting pack ice are less common, but have sampled a variety of regions intermittently over the past five decades (e.g., Langleben, 1971; Grenfell and Maykut, 1977; Perovich, 1991; Perovich et al., 2002; Nicolaus et al., 2010; Divine et al., 2015; Light et al., 2015; Xia et al., 2015). One of these studies (Impacts of Climate on the Eco-Systems and Chemistry of the Arctic Pacific Environment, "ICESCAPE", 2010, 2011; Arrigo, 2015) provided an extensive sampling of spectral albedo on first-year ice in the Chukchi and Beaufort Seas during the melt season (June, July). This study documented only snapshots of individual floes, as no one floe was followed. In contrast, year-long drift programs furnish unique opportunities for understanding processes in the context of a full annual cycle. The SHEBA expedition (1997–1998; Uttal et al., 2002) took place in the Beaufort Sea and provided a benchmark time series of α_{tot} and an extensive library of α_λ measurements for different surface types (Perovich et al., 2002). Twenty-two years later, the MOSAiC expedition (2019–2020) took place in the Central Arctic (**Figure 1**) and served as a platform for an unprecedented set of coordinated observations, including detailed albedo measurements. As SHEBA occurred in an Arctic dominated by perennial sea ice, measurements were made almost exclusively on multiyear ice. In contrast, MOSAiC was carried out in an Arctic dominated by much younger ice, and measurements were made exclusively on second- and first-year ice.

This manuscript presents surface-based spectral and broadband albedo observations for individual ice types,

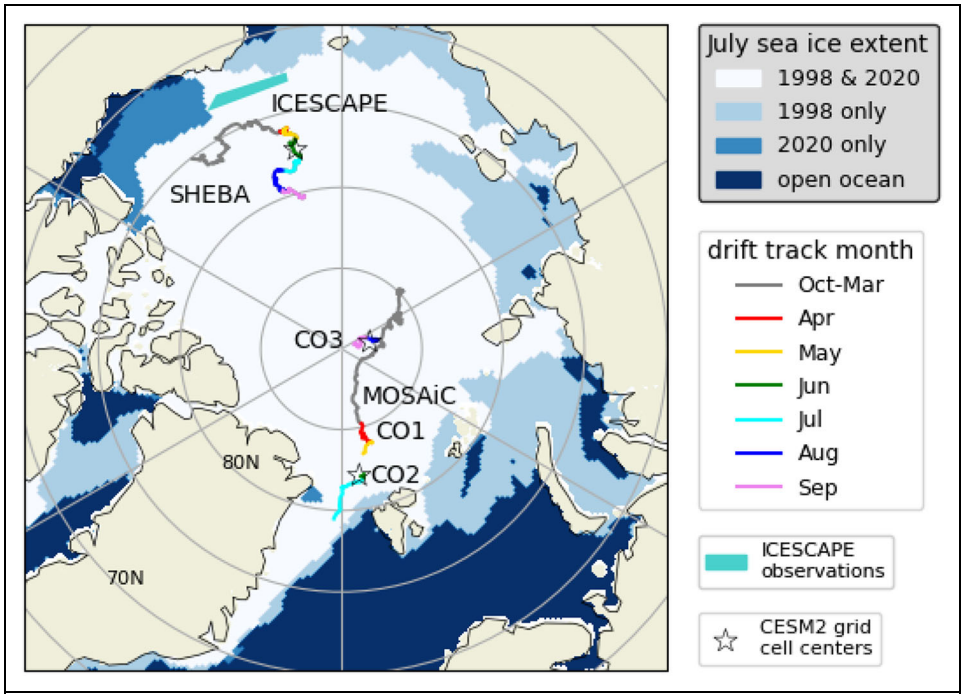

Figure 1. Map of sea ice extent, drift tracks, and model grid cell locations. Drift tracks indicated for MOSAiC (2019–2020) and SHEBA (1997–1998), as well as the sampling region of the ICESCAPE expedition (2010, 2011; teal shading). Colored drift segments indicate individual months during the sunlit season (April–September); gray segments indicate October–March drift. MOSAiC Central Observatories (CO1, CO2, CO3) are noted, and open stars indicate the center point of 1 degree × 1 degree CESM2 grid cells used in the analysis. July sea ice extent for SHEBA and MOSAiC are also indicated (Cavalieri et al., 1996, updated yearly).

along with estimates of aggregate albedo made along survey lines during the MOSAiC drift. The albedo measurements are supplemented by observations of the physical state of the snow and ice cover. Our aim is to understand the characteristic properties of key surface types and to assess the seasonal evolution of the albedo of a younger, thinner ice cover. We present representative spectral albedos of individual surface types, their spatial and temporal variability, and examine details of seasonal transitions. Comparison with observations from SHEBA and ICESCAPE, as well as model simulations, provide opportunities for model validation and improvement.

2. Methods

The MOSAiC drift experiment, operated from the Research Vessel *Polarstern* (AWI, 2017), was established on second-year ice in the northern Laptev Sea during October 2019 and roughly followed the Transpolar Drift across the eastern Arctic (**Figure 1**; see also Nicolaus et al., 2022). The experiment was designed to monitor a single "Central Observatory" (CO), consisting of ice proximal to the vessel, with the labor and logistics divided into operational "legs" for continuous manned observation. Nicolaus et al. (2022) detail the various measurements made by the Ice Team during each leg, which included intensive characterization of the sea ice and snow cover mass and radiative budgets, ice dynamics, and physical and optical properties. The sunlit season (April–September) spanned three operational legs: Leg 3 (February–May), Leg 4 (June–July), and Leg 5 (August–September).

Leg 3 was carried out on the original floe (CO1) which was composed of second-year ice, some of it containing areas of patchy sediment likely entrained when the ice grew on the Siberian shelf (Krumpen et al., 2020). Areas of open water proximal to CO1 grew new ice during the winter, providing access to first-year ice. Operations were suspended on May 12, just after a storm broke up the CO and the surrounding ice into numerous smaller floes. This dynamic event defined the end of Leg 3.

When R/V *Polarstern* returned to begin Leg 4 on 17 June, it returned to the same collection of floes as CO1, although repositioning the observatory to a more stable area within the CO1 was necessary due to strong ice dynamics. This new floe was designated CO2. Leg 4 was terminated on July 31 by advanced melt and proximity to the ice edge. In contrast to the drift continuity of CO1 and CO2, CO3 was established after an August gap on a first-year floe near the North Pole, beginning a new drift.

The optical measurement program began in April on CO1 during Leg 3. At this time, the snow cover was dry and cold. The transition to surface melt occurred during the May logistics gap. An autonomous station (L2, in the MOSAiC distributed network; see Nicolaus et al., 2022) left behind on a floe proximal to CO1 recorded hourly temperature and daily surface photographs. Measured air and snow surface temperatures first exceeded 0°C on May 26. The L2 surface image also indicated liquid droplets on the camera lens on this date, indicative of rain. Surface melt ponds appeared in the imagery beginning May 28, in accord with widespread ponding in satellite imagery

Table 1. Summary of on-ice albedo surveys carried out during the MOSAiC (2020) campaign

	MOSAiC (2020)			
Survey Information	**Leg 3 on CO1**	**Leg 4 on CO2**	**Leg 5 on CO3**	**SHEBA (1998)[b]**
Active dates	Apr 7–May 12	Jun 20–Jul 29	Aug 21–Sep 15	Apr 1–Sep 29
Ice type, total survey length (m)	First-year, 150; second-year, 200	First-year, 350; second-year, 200	First-year, 340	Multiyear, 200
Survey line name, ice type, total length (m), interval (m)	ROV3, First-year, 150, 10; SYI Line, second-year, 200, 10	Lemon Drop (LD), first-year, 200, 5; Root Beer Barrel (RBB), second-year, 200, 5; ROV4, first-year, 150, 5	Kinder, first-year, 200 (sheared to 140 on Aug 22), 5; ROV grid (Bounty), first-year, 60, 5; Toblerone, first-year, 140 (40 m spur on ridged ice), 5	Main albedo line, multiyear, 200, 2.5 (α_{tot}), 5 (α_{λ})
Albedo measurements	α_{tot}	α_{tot}, α_{λ}	α_{tot}, α_{λ}	α_{tot}, α_{λ}
Dates measured[a]	ROV3: Apr 7, 11, 17, 18, 22, 25, 29, May 2, 12; SYI: Apr 29, May 2, 12 (revisited Leg 4 **Jun 29**[a], **Jul 15)**	LD: **Jun 19**[a]**, 20, 21, 22, 24, 26, 30**, **Jul 6, 7, 13, 17, 21, 24, 29**; RBB: **Jun 19, 20, 21, 26, 30**, **Jul 6, 7, 13, 17, 21, 23, 27**; ROV4: **Jun 27, 28, Jul 4, 7, 10, 11, 14, 21, 28**	Kinder: **Aug 21**[a], **23**, **24**, **25**, **27**, **29**, **Sep 1**, **2**, **3**, **4**, **5**, **6**, **7**, **8**, **9**, **10**, **12**, **13**, **14**, **15, 16, 17, 19**; Bounty: **Aug 25**, **29**, **31**, **Sep 2**, **12, 19**; Toblerone: **Sep 6**, **8**, **11**, **12**, **15, 17, 19**	65 dates
Coordinated physical property measurements	Snow depth, ice thickness	Snow depth, pond depth, SSL thickness, total ice thickness	Snow depth, pond depth, SSL thickness, total ice thickness	Snow depth, pond depth, SSL thickness
Melt, freeze onset dates	May 26 (initial), Jun 9 (continuous)	(not applicable)	Aug 26 (initial), Sep 16 (continuous)	May 29

[a] Dates in bold indicate both broadband and spectral albedo measurements.

[b] From Perovich et al. (2002).

(Webster et al., 2022). Although snowfall and freezing conditions followed for a few days, more widespread ponding at L2 resumed on June 9, and remained approximately continuous for the remainder of the melt season. Optical measurements were carried out without interruption during the entire CO2 phase (Leg 4). After the August gap, optical measurements resumed at CO3 on August 21 to complete the annual cycle by capturing the return to freezing conditions. Optical measurements were curtailed on September 19.

The objective of the MOSAiC optics program was to quantify the partitioning of solar radiation in the sea ice system. A key component of this objective was a detailed description of the albedo of the ice cover through the sunlit season. **Table 1** provides an overview of the surface-based albedo measurements carried out at both MOSAiC and SHEBA on first-year, second-year, and multiyear ice types, including details of the individual MOSAiC survey lines at CO1, CO2, and CO3. Figure S1 shows airborne laser altimeter and optical drone imagery maps illustrating the locations of all albedo survey lines. These lines varied in length (60–200 m) and were sampled every 5–10 m. Efforts were made to create lines representative of the larger area by choosing terrain that appeared typical of each floe. The ROV3 (CO1) and ROV4 (CO2) lines overlay at least one edge of the under-ice ROV sample grid (see Nicolaus et al., 2022). Maintenance of uninterrupted survey lines for the entire annual cycle was not feasible due to the necessary CO repositioning in June and again in August. Albedo observations at additional locations targeting specific experiments will be addressed in future publications.

Measurements of α_{λ} were carried out using an Analytical Spectral Devices spectroradiometer equipped with a custom gooseneck cosine collector (Grenfell and Perovich, 2008) mounted on a 1.5-m hand-held carbon fiber boom. The observation of α_{λ} requires only measurement of the ratio of upwelling to downwelling irradiance, so radiometrically calibrated instrumentation is not necessary. Incident and reflected values were recorded serially, but as close together in time as possible, with ten scans taken for each. The albedo was calculated from the ratio of the average of the ten reflected scans to the average of the ten incident scans.

The spectral range of the α_{λ} measurements was 350–2500 nm with values sampled every 1.4–2 nm and interpolated to 1 nm. Quality control for α_{λ} included six steps (Smith et al., 2021a): i) a parabolic correction was applied to account for a temperature-related offset between sensors (applied between 750 and 1000 nm; see Hueni and

Bialek, 2017); ii) a flag quantifying the variability in incident solar radiation was used to exclude scans where the incoming radiation at 600 nm changed by more than 20% between subsequent scans; iii) albedos with physically unrealistic slopes (e.g., negative slope between 400 nm and 450 nm) were removed; iv) noisy parts of the spectrum were filtered and removed, specifically wavelength bands where the rolling standard deviation (20 nm wide window) was greater than 0.02; v) values at near-infrared wavelengths were smoothed with rolling means (1200–1800 nm were smoothed with a 15-nm wide window and values at wavelength longer than 1800 nm were smoothed with a 30-nm window); and vi) all albedos with value greater than unity or less than zero were removed. Albedos were reported with precision of three significant figures; however, the expected accuracy is unlikely to exceed two significant figures in the best circumstances.

Measurements of α_{tot} were carried out using a Kipp and Zonen albedometer, also mounted on a hand-held boom, with effective spectral range of 300–3000 nm. Analogous to the spectral values, α_{tot} was calculated from the ratio of reflected to incident irradiance. The broadband albedo dataset includes two quality metrics: i) error associated with low-light conditions and resolution of the instrument (defined as the difference between the maximum and minimum albedo associated with a deviation of 0.01 in both values); and ii) degree of variability associated with rapidly changing light conditions, where the change in incoming radiation from observations before and/or after is calculated as a percent of the measured incoming radiation. These metrics were not used to remove any of the α_{tot} data presented here, but are included in the archived dataset, where full description of the procedures and code used to process both α_{λ} and α_{tot} can be found (Smith et al., 2021a; 2021b).

During Leg 3, instrumentation to measure α_{λ} was not available at the station, so albedo surveys were restricted to α_{tot}. During Legs 4 and 5, simultaneous measurement of α_{λ} and α_{tot} were collected along all optical survey lines. Both α_{λ} and α_{tot} were measured approximately 1 m above the surface, yielding an instrument footprint of approximately 2-m radius (with 90% of total upwelling light measured originating from within 2-m radius of the sensor position). During the summer melt season, the surface within a single field of view frequently contained mixed surface types, but areas with approximately homogeneous surface conditions within the radiometer field of view were selected to represent individual surface types. Measurements were made along survey lines every 5 m (Legs 4 and 5) or 10 m (Leg 3), and always on the same side of the line to avoid disturbing the targeted surface. Albedo measurements were generally carried out as close to solar noon as practical. Time of day (solar zenith angle) and cloud and meteorological conditions were noted.

Surface characterization methods included manual measurements of snow depth, approximate surface scattering layer thickness, and melt pond depth (Smith et al., 2021a; 2021b). Digital photos were taken at nearly all albedo measurement locations on each sampling date (Smith et al., 2021c). Routine total (snow and ice) thickness measurements were made parallel to Lemon Drop (LD), Root Beer Barrel (RBB), and Kinder lines offset by approximately 1–2 m using a non-destructive electromagnetic induction sounding detector (GEM-2; Hunkeler, 2016; Hunkeler et al., 2016), coincident with snow and pond depth surveys using a Magnaprobe depth detector (Sturm and Holmgren, 2018; Itkin et al., 2021; Webster et al., 2022). While these transects were not precisely co-located with the albedo measurements (to avoid disturbing the surface of the albedo sensor footprint), they are useful for developing an understanding of the surface state and ice thickness distribution and evolution. Additionally, manual sampling for snow depth, pond depth, pond ice lid thickness, and sea ice thickness was done directly on certain albedo survey lines at the completion of Leg 4 (RBB) and Leg 5 (Kinder and Bounty). Furthermore, snow structure was quantified using a SnowMicroPen (Schneebeli and Johnson, 1998) and ice samples were collected at each survey line for imaging by onboard micro-computed x-ray tomography (see Nicolaus et al., 2022).

To provide context for these measurements, we compare them with albedo measurements made on drifting pack ice during two previous expeditions. During the year-long SHEBA drift (**Figure 1**; October 1997–October 1998) albedo data were collected on a single survey line from April through September 1998. Similar to MOSAiC, the line was surveyed using the same Kipp and Zonen system for estimation of α_{tot} (every 2.5 m) and previous generation spectroradiometers (separate Spectron Engineering instruments for visible (SE-500) and near-infrared (SE-1400) wavelength ranges) for estimation of α_{λ} (every 5.0 m). The ICESCAPE mission (**Figure 1**; June–July 2010 and June–July 2011) was carried out on first-year ice in the Chukchi and Beaufort seas. There was no drift component to the ICESCAPE mission, so no specific measurement sites were revisited and no survey lines were installed. Measurements of α_{λ} for this expedition represent independent samples at sites on selected floes (Light et al., 2015). No α_{tot} measurements were made during ICESCAPE.

Comparison with output from a global climate model was also carried out to provide insight into the use of these observations to improve predictive capability of future climate. CESM2 is a comprehensive Earth System Model that has a nominal 1° resolution for the atmosphere, ocean, and sea ice components (Danabasoglu et al., 2020). As shown by DuVivier et al. (2020), the Arctic sea ice in standard CESM2 simulations is somewhat thin relative to observations. As a consequence, modest tuning of the snow optical properties was performed to improve the Arctic sea ice state with little consequence for other aspects of the CESM2 simulated climate (Kay et al., 2022).

3. Results and discussion

3.1. Representative albedos of individual surface types

Figure 2 shows representative values of α_{λ} plotted as a function of wavelength, along with corresponding photographs of individual surface types characterized in this study. These representative spectra were chosen from

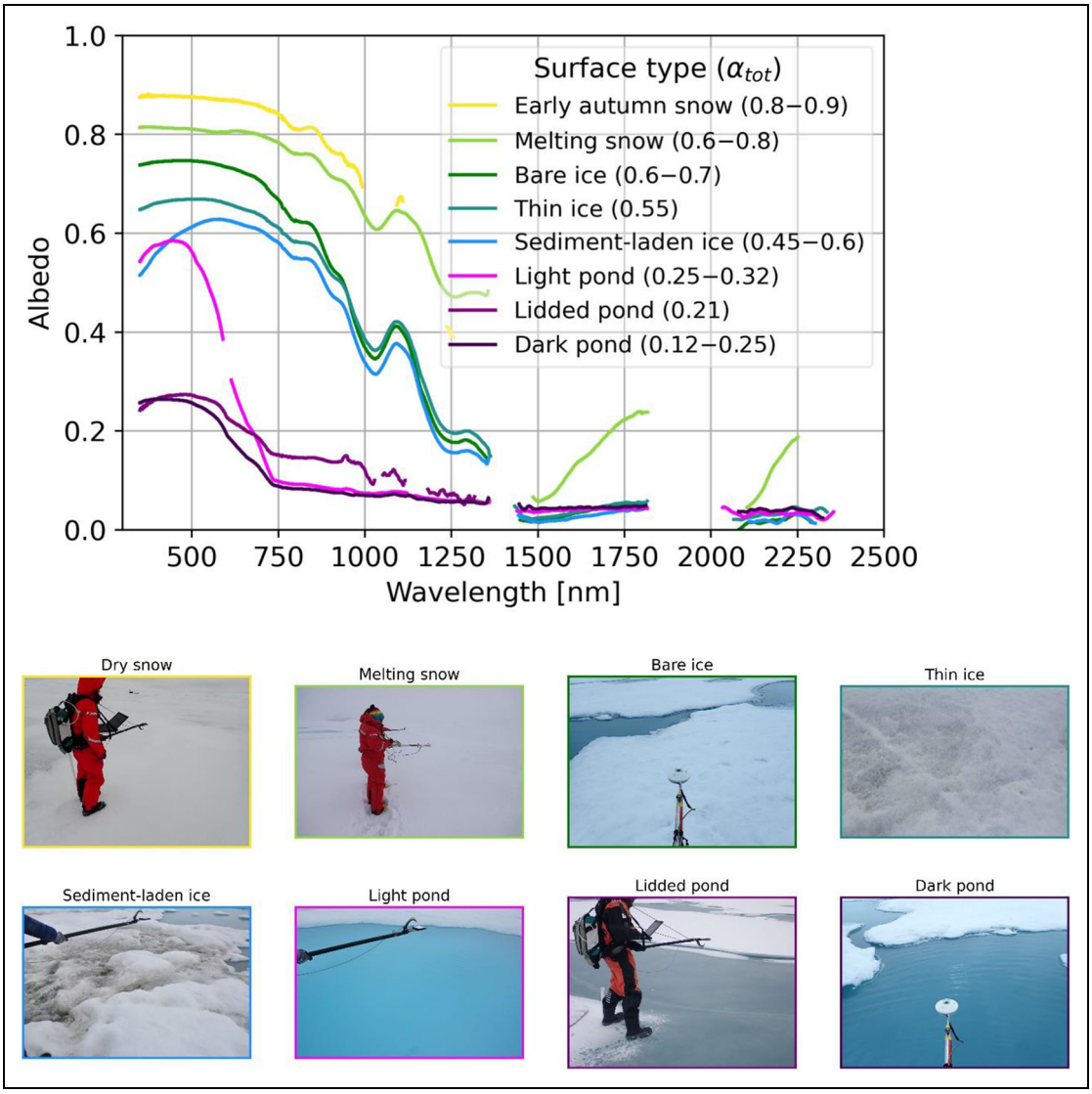

Figure 2. Representative spectral albedos for individual ice surface types. Measurements include α_λ curves and range of α_{tot} values (inset legend) for eight individual surface types. Thin ice and lidded pond values represent example values; full range of values not specified. Photographs show measurement sites corresponding to each curve.

the complement of survey line positions that had approximately uniform appearance within the instrument footprint. Not all surface types are present simultaneously, as their distribution evolves over the course of the sunlit season. The following sections present albedos representative of: 1) snow on sea ice; 2) bare, melting sea ice; 3) ponded sea ice; 4) thinning bare, melting sea ice; and 5) sediment-laden sea ice.

3.1.1. Snow on sea ice

As the sun rose at the MOSAiC CO1, the snowpack was cold and dry, with an average thickness (± standard deviation) of 0.32 m ± 0.18 m (n = 1486; Itkin et al., 2021) and well-characterized history (Nicolaus et al., 2022). Optical surveys of α_{tot} were conducted at CO1 along a 200-m long line ("ROV3") and on the "SYI" line (Figure S1). These measurements took place in freezing conditions, prior to any ephemeral or continuous surface melt.

The light green curve in **Figure 2** shows representative α_λ for a case of melting snow measured early on Leg 4 (June 20, LD 165 m). This α_λ is significantly smaller than that for cold, dry spring snow (Grenfell and Maykut, 1977), as the grains were large and liquid water between grains reduced total scattering. These effects are noted primarily at wavelengths shorter than 1000 nm. Albedos remained relatively high in the wavelength range of 1500–1850 nm, as backscatter from the surface-most snow grains remained significant. The range of α_{tot} is 0.6–0.8.

In August and September, values for α_λ and α_{tot} were surveyed for freshly accumulating snow on CO3. The snow at CO3 was thinner and warmer than the spring snow pack observed on CO1. The yellow curve in **Figure 2** shows a representative α_λ for accumulating snow (depth of 0.1 m) measured at the 20-m position on Kinder Line on September 17. The range of α_{tot} values observed for this autumnal snow (CO3) was 0.8–0.9 (inset legend, **Figure 2**). This range includes the snow that fell during freeze up which was frequently subject to temperature fluctuations around freezing, variable underlying surface conditions, and mixed phase precipitation. Low light levels during

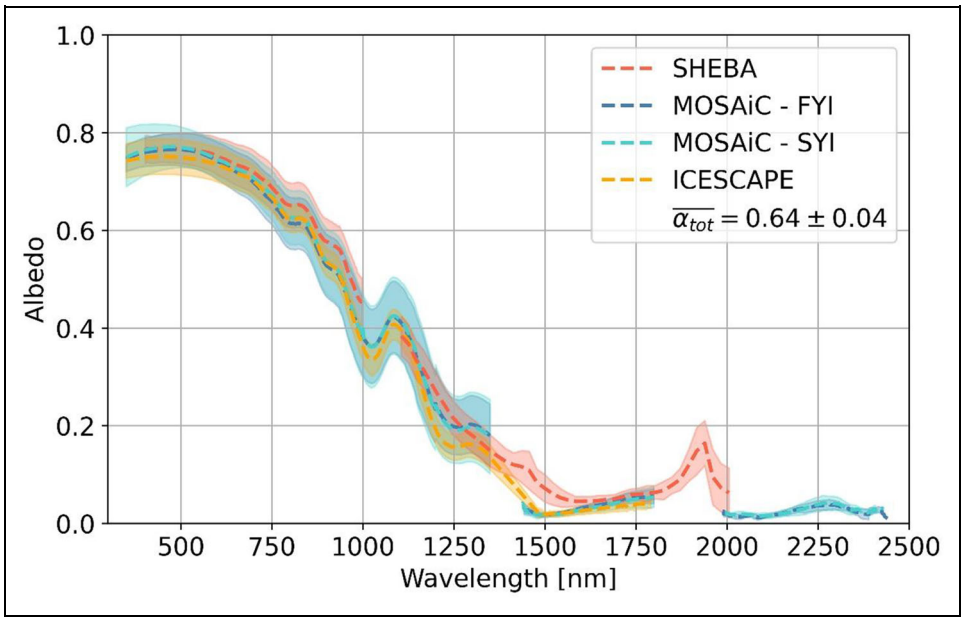

Figure 3. Average spectral albedo for thick, bare, melting sea ice. Average for first-year ice (dark blue, n = 30) and second-year ice (light blue, n = 25) observed during MOSAiC (2020), multiyear ice (red, n = 26) observed at SHEBA (1998), and first-year ice (gold, n = 14) observed during ICESCAPE (2010, 2011). Color-corresponding shading indicates one standard deviation in measured albedo. Average total albedo for all MOSAiC measurements is 0.64 ± 0.04.

August and September caused upwelling irradiance measurements to have low signal-to-noise ratio, thus measurements at wavelengths longer than 1250 nm during this time generally did not pass quality control.

3.1.2. Bare, melting sea ice

Once the snow ablates, the melting sea ice surface is exposed. When this melting, bare sea ice develops a rough, coarse-grained surface, it has a representative α_λ as shown in **Figure 2** (dark green curve; observed range for α_{tot} of 0.6–0.7). Representative α_λ values were high at visible wavelengths, but decreased rapidly at near-infrared wavelengths relative to snow.

Figure 3 shows the average observed α_λ as a function of wavelength for bare, melting sea ice observed during MOSAiC (first- and second-year ice), SHEBA (multiyear ice), and ICESCAPE (first-year ice). Standard deviations for each curve in the figure are relatively small, suggesting that for any specific summer, α_λ for melting bare ice is relatively constant. This small variability of α_λ observed at SHEBA was noted by Perovich et al. (2002). The average independently observed α_{tot} for the thick, bare, melting ice measured at MOSAiC was 0.64 ± 0.04 (**Figure 3**).

Besides the small standard deviations for each curve, the three curves are almost identical, suggesting that the albedo of bare, melting sea ice appears to be relatively invariant geographically (Central Arctic Ocean, Beaufort Sea, Chukchi Sea) over a 22-year span (1998–2020). This result indicates that bare, melting sea ice develops and maintains inherent optical properties that are fundamental to this surface type and are not sensitive to the histories of ice evolution or atmospheric forcing, at least as long as some minimum ice thickness is maintained.

Perhaps most notable is that α_λ for bare, melting ice also appears invariant with respect to ice age (first-year, second-year, multiyear). We suggest that the principal reason for this invariance is the ubiquitous presence of surface scattering layers (SSLs) on bare, melting sea ice (see Untersteiner, 1961; Grenfell and Maykut, 1977; Zubov, 1979; Eicken et al., 1995; Tucker et al., 1999; Perovich et al., 2001; Perovich et al., 2002; Nicolaus et al., 2012; Light et al., 2015; Katlein et al., 2019). This layer is defined as the coarse-grained, crumbly, well-drained uppermost portion (approximately 0.02–0.05 m) of the ice. Large, numerous grains cause this layer to have light scattering properties similar to coarse-grained snow. While there is no discrete lower boundary to this scattering layer, the magnitude of scattering gradually decreases until the freeboard level. This SSL is generally understood to be formed and maintained by absorbed solar radiation and subsequent drainage of meltwater. When manually removed by shoveling or scraping, it was observed to re-form within a day (see Perovich et al., 2001). It appears to form on the sea ice surface beneath melting snow and persist through summer.

Qualitative observations made during SHEBA suggest that the SSL physical thickness typically increases on sunny days and decreases on cloudy days (Perovich et al., 2002), but these observations did not suggest that the physical depth nor the characteristic grain size of the SSL evolve systematically over the course of the melt season. Light et al. (2008) estimated scattering coefficients within the SSL to be typically two orders of magnitude larger than interior ice (below freeboard), but there is no physical reason to expect them to be uniform across a floe or a region. Details of the structural and optical properties of SSLs are difficult to measure. This is partly a sampling

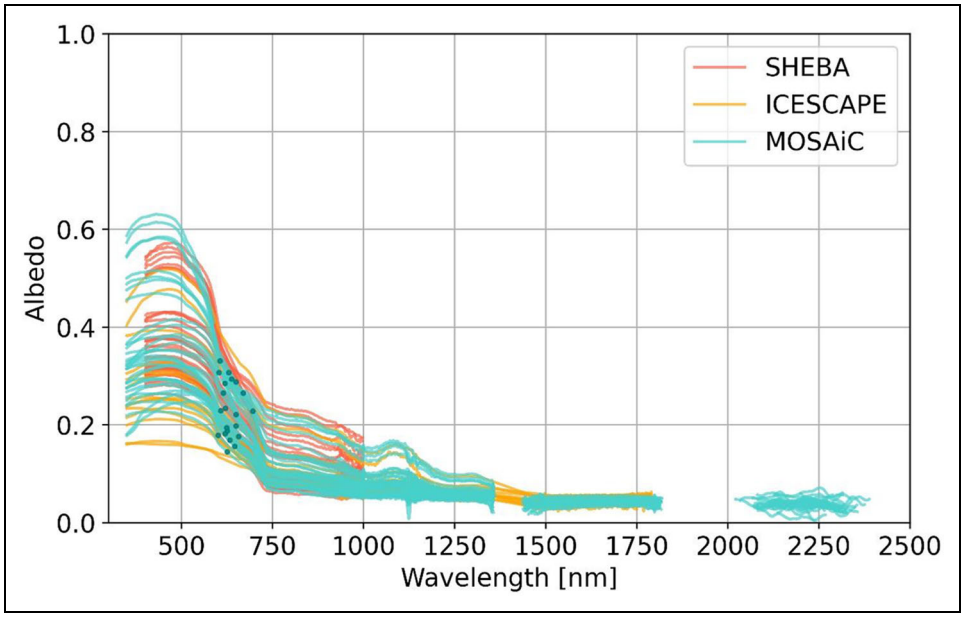

Figure 4. Spectral albedo measurements for ponded ice. Spectral albedos for ponded ice measured at MOSAiC (teal), SHEBA (orange), and ICESCAPE (gold). Dark teal points indicate magnitude of independently measured total albedo (MOSAiC only) associated with each spectral measurement and are plotted at the intersecting wavelength.

problem, as the SSL is fragile, rarely survives coring, and, if it does get sampled, is difficult to handle and document using traditional techniques for characterizing ice and snow. During MOSAiC, efforts were made to estimate the thickness and characteristic grain size of the SSL (A Macfarlane, personal communication, December 2020; Nicolaus et al., 2022).

While the spectral albedo of thick, snow-free melting sea ice appears remarkably steady, there appear slight spectral differences between the different ice types at different field stations (**Figure 3**). We suspect these are artifacts related to differences in spectroradiometer instrumentation or post-processing methods, rather than physical differences of the ice. In particular, we note that the wavelength interval 1,300–1,400 nm is noisy due to atmospheric absorption features, and that these data were removed during quality control for the MOSAiC dataset, but smoothed in the ICESCAPE dataset. The measurements made during ICESCAPE were carried out under conditions with likely larger incident irradiance, owing to the lower latitude and closer timing to summer solstice. Additionally, the peak observed in α_λ from SHEBA between 1800 nm and 2000 nm was not observed in the MOSAiC observations as a result of more stringent quality control in the MOSAiC data processing, which resulted in no data in this band due to high noise. The cause for this peak in the SHEBA observations is not clear.

3.1.3. Ponded ice

Ponded sea ice is physically and optically distinct from bare ice. Ponded ice has consistently smaller albedo than bare ice because the highly scattering SSL of bare ice is replaced by puddled liquid water which absorbs light but has negligible scattering (pink and purple curves in **Figure 2**). We classify ponds as "light" (pink curve) or "dark" (purple curve) even though the distinction between these two optical classes of melt pond is somewhat arbitrary, and is neither exclusive nor exhaustive. As presented here, dark ponds have $\alpha_{tot} < 0.25$ and light ponds have $\alpha_{tot} > 0.25$.

Figure 4 shows α_λ measurements for ponded ice made during MOSAiC, SHEBA, and ICESCAPE. Identifying representative ponds for a region is challenging given the significant spatial and temporal heterogeneity. Dark ponds often occur late in summer, during advanced melt, and are typical of undeformed first-year ice. Light ponds tend to form on thicker sea ice, especially where the pond floor may contain retextured snow, which retains significant scattering. Also, a mixture of ponded ice shades can occur within the same pond and within the same floe, where one area is significantly lighter blue than other areas.

The α_λ values for ponded ice shown in **Figure 4** have high variability at visible wavelengths (400–700 nm) at all three field experiments. Because visible light is weakly absorbed by the standing water, the albedo at these wavelengths is ultimately determined by the optical properties of the pond floor. Floors with large thickness, rafted ice, or high bubble density often produce enough scattering to give the pond a "light" appearance and higher albedo. Where the pond floor was once snow, as is typical on the flanks of ridges, bubbles are often retained and these ponds typically have bright, light blue color.

Ponds become "dark" when the underlying ice has low scattering. The floors of such "dark" ponds are typically composed of the ice beneath freeboard, "interior ice", which is known to have a scattering coefficient of at least one, often two, orders of magnitude smaller than the SSL (Light et al., 2008). Additionally, layers of rotten ice sometimes form within pond floors during advanced melt, but,

because this ice is submerged, its interfaces are typically flooded and scattering is limited.

Despite large variability at visible wavelengths, ponded ice has small variability at near infrared wavelengths ($\lambda >$ 700 nm). Here, α_λ is dominated by absorption in the pond water. Values of α_λ for ponds at near-infrared wavelengths were observed to be consistently below 0.3. The albedo is augmented by Fresnel reflection at the pond surface, and this factor determines a steady albedo value $\leq$ 0.1 at wavelengths longer than 1,200 nm. On sunny days, a specular reflection can be seen on pond surfaces which can significantly enhance the albedo (for example, along RBB line on July 27, not shown).

Ponds observed during MOSAiC (both Legs 4 and 5; teal curves in **Figure 4**) show a larger range of α_λ than was observed at either SHEBA or ICESCAPE. The ponds observed at ICESCAPE (gold curves in **Figure 4**) were measured exclusively on first-year ice and appear to be generally darker, likely because the measurements were made mostly on thinner, undeformed first-year ice where the thickness of the pond floor was typically less than 1 m and had relatively little scattering. Only two "light" ponds were recorded during ICESCAPE. Ponds observed at SHEBA (orange curves in **Figure 4**) occurred exclusively on multiyear ice and appeared to have α_λ values generally higher than the ponds observed on first-year ice during ICESCAPE, possibly representative of the thicker multiyear ice that was prevalent. Values of α_λ for ponds measured during MOSAiC and SHEBA spanned similar ranges, though the averages were different, likely due to a distribution of pond floor optical properties and floor thickness.

Also indicated on each α_λ curve for MOSAiC is the magnitude of the corresponding α_{tot} measurement (dark teal points in **Figure 4**). In each case, α_{tot} is plotted at the wavelength where its magnitude intersects the associated α_λ curve. These values are useful for reconciling estimates of computed and measured total albedo in the absence of spectral downwelling incident irradiance measurements.

3.1.4. Thinning bare ice

Model simulations (Grenfell, 1979; Briegleb and Light, 2007) suggest that when the thickness of bare, melting sea ice is less than about 1 m, the ice becomes thin enough for the albedo to develop optical sensitivity to the low backscatter of the underlying ocean. Observations of thin ice (Perovich and Grenfell, 1981; Brandt et al., 2005; Taskjelle et al., 2016) concur, but these studies were carried out on young, growing ice and do not account for a fully developed SSL on the ice surface, as would be expected for summer ice.

Due in part to the dynamic activity at CO2 during the end of the melt season, there was limited opportunity to monitor albedo as the ice thinned into this regime. One albedo measurement was made along the ROV4 survey line where the ice thickness was estimated to be approximately 0.40 m ($\alpha_{tot} = 0.55$; teal curve in **Figure 2**). The observed α_λ had reduced values at visible wavelengths, resulting from reduced total scattering of the ice at this location. At wavelengths longer than about 900 nm, α_λ was approximately the same as for thicker ice, likely due to the remaining SSL. This measurement does not define a unique surface type, so it should not be taken as a representative albedo for thin ice, but rather provides an illustration of the decreased α_λ resulting from ice with decreased physical and optical thickness.

3.1.5. Sediment-laden ice

Absorbing constituents entrained within sea ice can strongly affect the partitioning of incident sunlight. Such absorbers include pigments associated with biota (Mundy et al., 2007), deposited black carbon and other aerosols (Goldenson et al., 2012), and sediments entrained during ice growth (Reimnitz, 1994; Light et al., 1998). Areas of CO1 and CO2 contained significant sediment inclusions (Krumpen et al., 2020), and some of the optical effects of this material were captured in the albedo surveys at CO2. Bare, melting sediment-laden sea ice is characterized by an α_λ (light blue curve in **Figure 2**) that is smaller than that for bare, melting clean ice (dark green curve in **Figure 2**). The most prevalent signatures of entrained sediment within sea ice are: i) the wavelength of maximum albedo, which typically occurs at wavelengths greater than about 500 nm when significant amounts of sediment are present within the upper layers of the ice; and ii) the sharp decrease in α_λ at blue wavelengths due to enhanced absorption by mineral material.

Figure 5 shows a progression of selected α_λ values for sediment-laden ice observed along the RBB line (45 m) during Leg 4. Early in the progression (dark and medium blue curves, representing June 21 and 30, respectively), some melting snow was still present on the ice surface resulting in albedos on these two dates being consistently higher than the albedo of bare, melting ice. Sediment within the ice was first noted at this time, as the influence of the enhanced absorption at all wavelengths can be seen in the June 30 measurement. As the snow melted and the ice surface ablated, entrained sediment gradually became exposed at the surface (light green and orange curves, representing July 13 and 21, respectively, in **Figure 5**). Corresponding α_λ values show decreasing values at all wavelengths and increased wavelength of peak albedo. Absorption by dark sediment at the surface caused enhanced ice ablation; the surface became patchy, and an uneven, hummocky surface developed (surface photos from July 13 and 23 in **Figure 5**). In some areas, small amounts of liquid water (approximate millimeter scale depth) accumulated as well. Further surface ablation resulted in concentration of sediment material in low points, with significantly reduced albedo (dark red curve, representing July 23, and corresponding photo in **Figure 5**).

3.2. Spatial and temporal variability

3.2.1. Variability on individual survey lines

As the ice cover progressed through spring, melt onset, summer, and freeze onset, the albedo responded with changes in both magnitude and spatial variability. **Figure 6** shows α_{tot} as a function of along-line position for each measurement day from all lines on each leg, with corresponding aerial photographs over the survey lines at

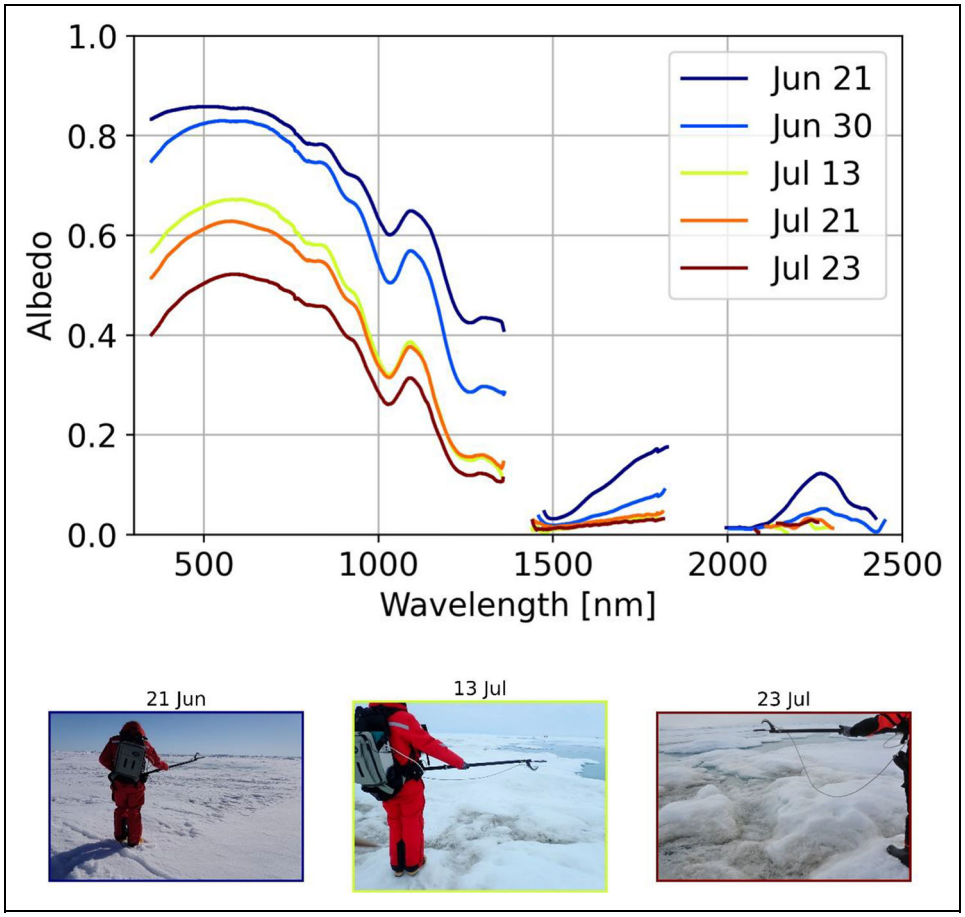

Figure 5. Melt season albedo progression for sediment laden sea ice. Spectral albedo observations recorded at 45 m on the RBB survey line for five dates during Leg 4. Corresponding surface photos for three dates indicate shoaling and accumulation of sediment material.

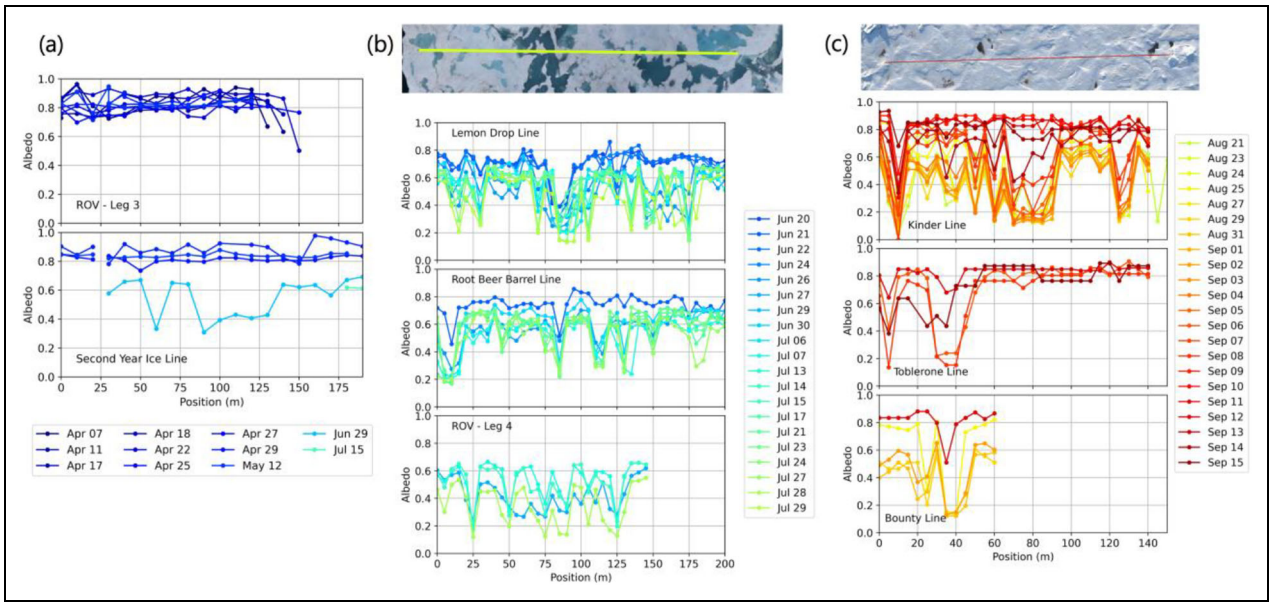

Figure 6. Spatially and temporally resolved total albedo measured on all MOSAiC albedo survey lines. Each curve represents the total albedo measured along a single survey line on selected dates, with line position on x-axes (m), measured total albedo on y-axes during (a) Leg 3 (CO1), (b) Leg 4 (CO2), and (c) Leg 5 (CO3). Also shown are aerial images for Lemon Drop Line (July 22) and Kinder Line (Sept 11) annotated with the locations of the respective survey lines (N Neckel, personal communication).

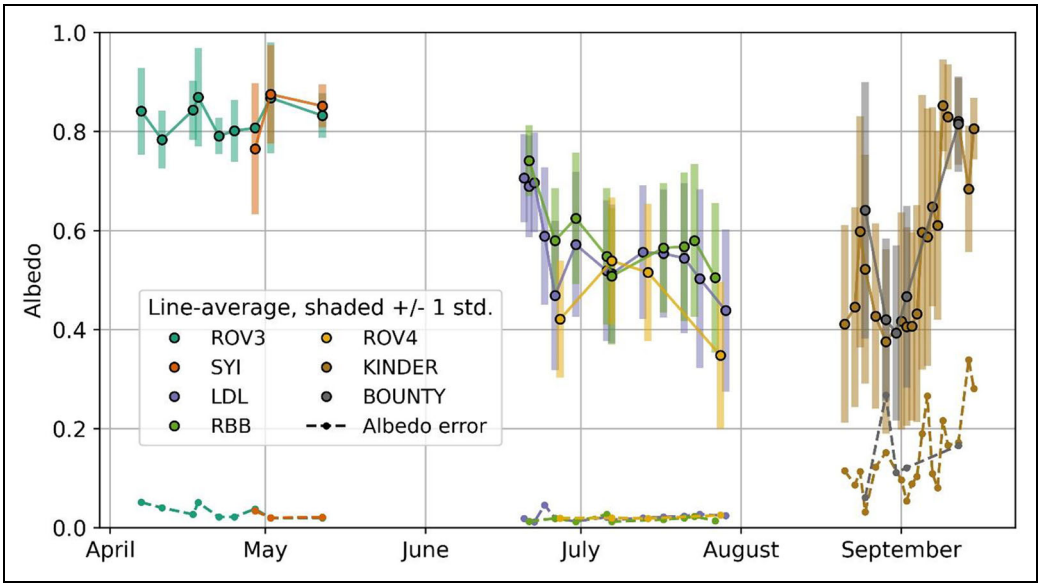

Figure 7. Temporal evolution of total albedo averaged over all positions on each survey line. Average albedo for each survey line (symbols) as function of time for the MOSAiC total albedo dataset, with one standard deviation (shaded bars) and estimated measurement errors (dashed lines) due to instrument sensitivity. Note increasing measurement error in September in response to decreasing light levels. The two gaps in the time series are shown for mid-May to mid-June and the end of July to mid-August.

CO2 (July 22) and CO3 (Sept 11) showing snapshots of the best characterized lines (LD and Kinder) from each leg. While the albedo was only sampled at discrete locations on these lines (5-m interval), there is clear correlation between the bright, bare ice areas on the images and the high α_{tot} areas on the surveys, and between the darker, ponded areas and lower α_{tot}. The image for CO2 illustrates the presence of both light (0–25 m; 175–200 m) and dark ponds (80–90 m) on the LD survey line. The progressive darkening of ponded ice throughout the melt season can be seen as decreasing α_{tot} values (**Figure 6b**), while the impact of freeze up and accumulated snowfall can be seen as increasing α_{tot} (**Figure 6c**). The measurement errors also increased during autumn due to low light levels and low solar elevation, suggesting that the albedo very close to zero measured at the 10-m position had large uncertainty.

The seasonal progression of α_{tot}, averaged over each of the seven survey lines, is shown in **Figure 7**, along with standard deviation and estimated measurement errors. The three different time intervals over which these data were collected distinctly show three of the temporal evolution phases described by Perovich et al. (2002). Leg 3 (CO1) measurements document the variability of dry, cold snow albedo, which had line-averaged α_{tot} values between 0.76 and 0.88 (CO1 only). The melt onset phase occurred during the May–June logistics gap. Leg 4 (CO2) measurements describe the albedo during the interval from the melt of remnant snow through the pond development phase, including pond drainage. Here α_{tot} values decreased with time as the ice surface transitioned from melting snow to both bare and ponded surface types. The second logistics gap occurred towards the end of the pond evolution phase close in time to the end of the melt season. Leg 5 (CO3) measurements describe the albedo during fall freeze up, and are characterized by variable weather conditions, which caused ponds to freeze surface lids, snow to accumulate, transient melt events, and a rain-on-snow event. In general, differences between the individual survey lines measured during a given leg (solid lines) are small relative to the spatial variability represented by individual time series (shaded bars in **Figure 7**). These small differences suggest that the survey lines captured the significant spatial variability in albedo that existed across each floe.

3.2.2. Temporal variability of bare, melting and ponded surface types

At the beginning of the melt season, liquid water collected at the ice surface, beneath the snow, forming areas with "subnivean" ponds (Webster et al., 2022). Areas where no ponds form developed a nascent SSL. Because these two precursor surfaces appear to underpin the trajectories of what ultimately determines the surface radiative balance of the summer ice cover, we assessed the optical factors that shape these two paths in **Figure 8**. Panel (a) shows spectral albedos for two positions on the LD line (**Figure 8**; 165 m solid curves; 175 m dashed curves). Initially, both positions were characterized as melting snow and had approximately identical albedo on June 20 (dark blue curves in **Figure 8**). Surface observations noted no indication that these specific positions had been ponded previously, in late May–early June, as the surface imagery taken at L2 and by satellite had suggested for some areas (shown in Section 2). Areas on first-year ice that had been ponded previously presented as shallow puddles of liquid water with thin ice lids, all beneath the fresh snowfall. By the end of June, however, the sites at 165 m and 175 m

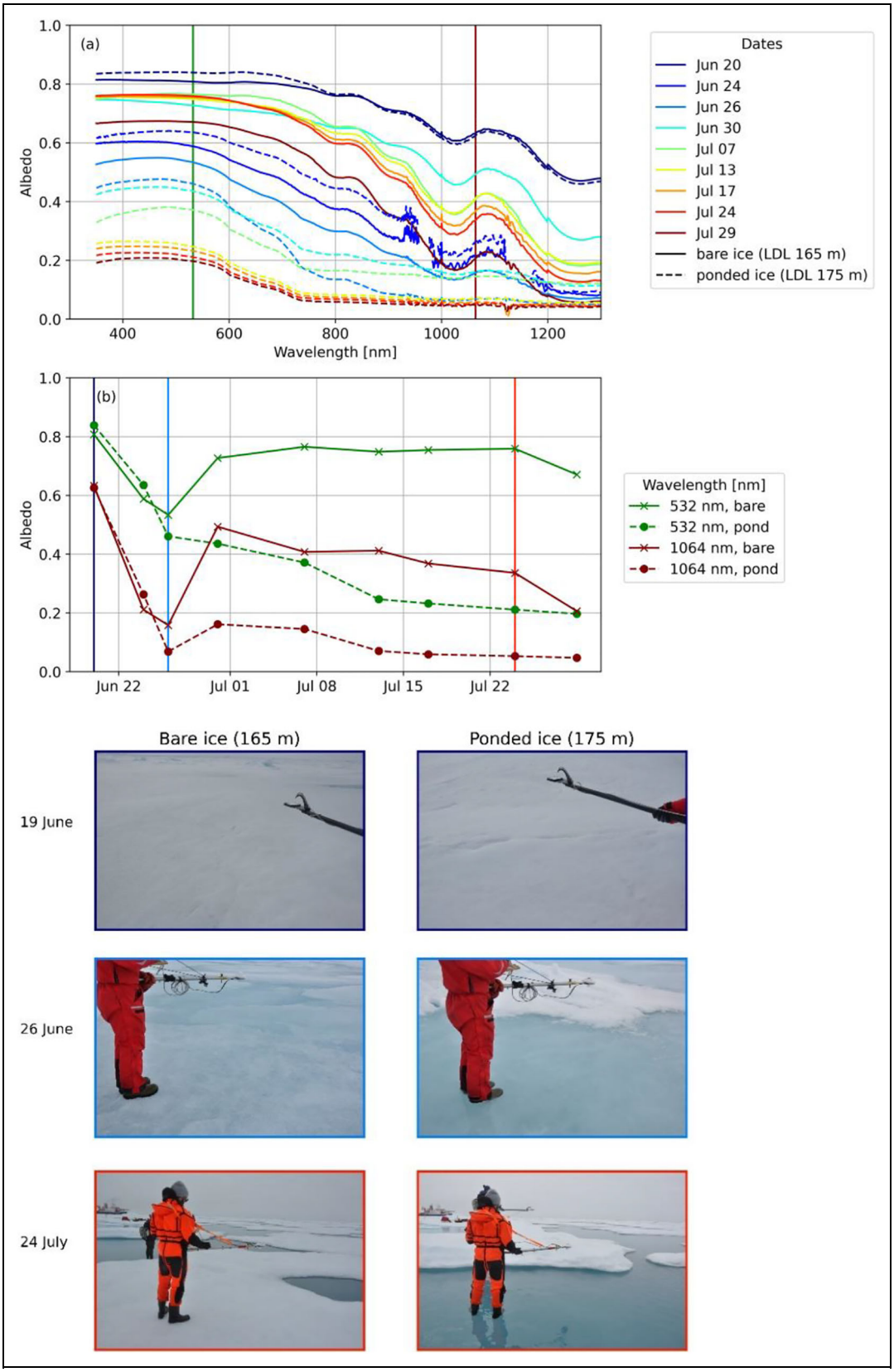

Figure 8. Spectral albedos documenting formation of bare, melting ice and ponded ice. Albedos at adjacent positions on the Lemon Drop line show evolution for bare (165 m; solid curve) and ponded ice at (175 m; dashed). Panel (a) shows the magnitude of the spectral albedos; (b) shows the time evolution of these albedos at wavelengths relevant for satellite altimetry: 532 nm (ICESat-2) and 1,064 nm (ICESat).

were clearly distinguishable as bare, melting ice and ponded ice. By mid-July the pond was a "dark" pond. At what point in this evolution did it become clear that one of these sites would become a pond, and the other bare ice?

By June 26, the albedos of both positions decreased as a result of the accumulation of liquid water. At 175 m, the liquid water pooled on the ice surface. At 165 m, the pooled water was beneath snow, resulting in slightly higher albedo. Not clear is whether small differences in elevation drove the accumulation of melt water and subsequent albedo difference, or the slightly lower albedo at 175 m forced additional heating, accelerating melt, and a localized albedo feedback response. At 175 m, a combination of these processes may have acted to accumulate liquid water and further reduce the albedo. Regardless, melt water continued to accumulate at the 175-m position, and by June 30, this position was clearly ponded and the surface at 165 m clearly bare. The 165-m position formed an SSL and had an albedo consistent with α_λ for bare, melting sea ice (July 24, light red curve in **Figure 8**). In contrast, the ice at 175 m continued to accumulate liquid water and had α_λ characteristic of a dark pond. Albedos of established ponds generally decrease with time, only increasing when the surface begins to freeze. Ponds can be expected to experience some drainage, which can significantly reduce pond size, but drainage rarely eliminates ponds completely. An instance of such drainage is seen at the 80-m position of LD (**Figure 6b**) where the pond retreated after the July drainage event. Here the area that was once ponded became bare and developed an SSL.

The evolution of these two surface types also has implications for the interpretation of remotely sensed surface imagery and lidar returns. **Figure 8b** shows a time series of the albedos of these two positions (165 m and 175 m on LD) at 1,064 nm and 532 nm, the wavelengths used by laser altimeters aboard ICESat and ICESat-2, respectively. The two study locations were indistinct at both wavelengths at the beginning of melt (June 20; **Figure 8**). Within days, snow melt caused the albedo at both wavelengths to drop rapidly. By June 26, the pond was clearly established, with albedo notably smaller at both wavelengths than the bare ice case. The bare ice albedo rebounded as the snow melted away and an SSL formed (evident by June 30). After this time, the pond albedo continued to decrease. The bare ice albedo remained largely constant, particularly at 532 nm. Albedos at 1,064 nm are more sensitive to the presence of liquid water, and larger albedo variability is likely a response to variations in liquid water at the ice surface. The pond location at 175 m reached the characteristic minimum 1,064 nm albedo value for ponded ice (0.1) by July 13.

3.2.3. Melt and freeze transitions

Aspects of the spatial variability and temporal evolution of α_λ are presented in **Figure 9** for a melting progression along the LD line on CO2 and a freezing progression along the Kinder line on CO3. Each figure panel represents

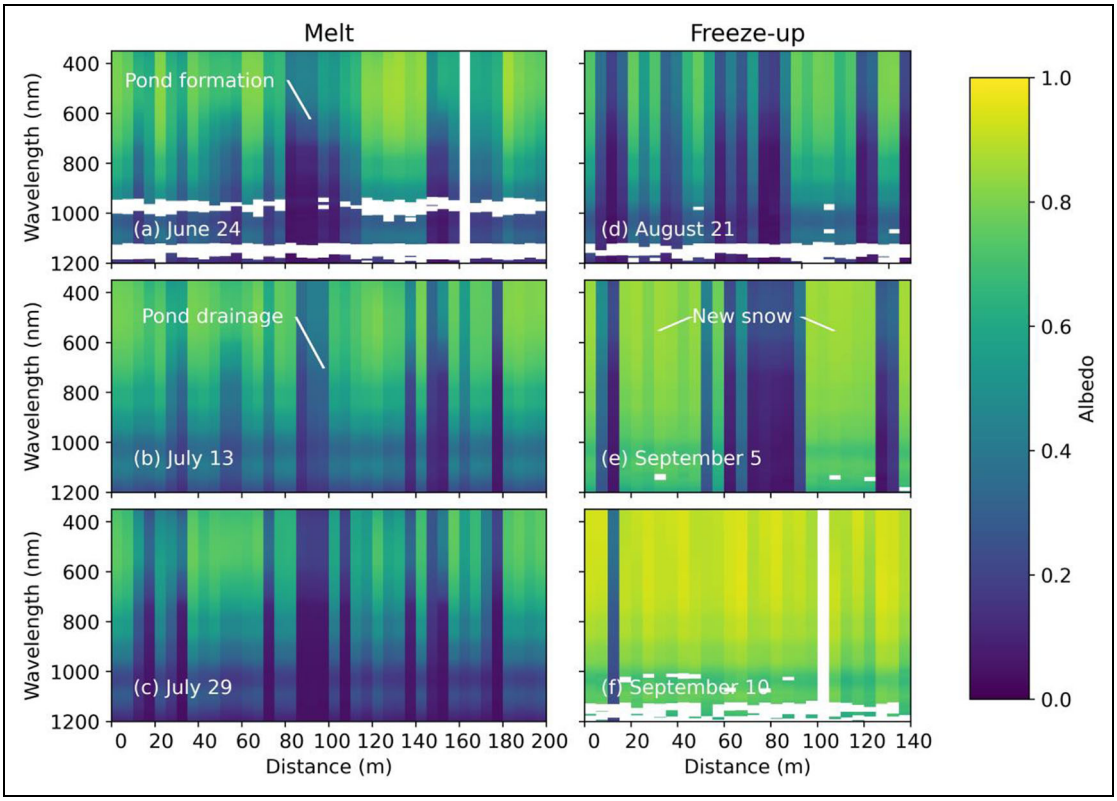

Figure 9. Spectral albedo for melting and freezing progression. Color maps depict the magnitude of the measured albedo as a function of line position (x-axes, m) and wavelength (y-axes, 350–1,200 nm). Left panels (a–c) show melting along Lemon Drop Line (June 24, July 13, and July 29); right panels (d–f) show freezing along Kinder Line (Aug 21, Sept 5, Sept 10).

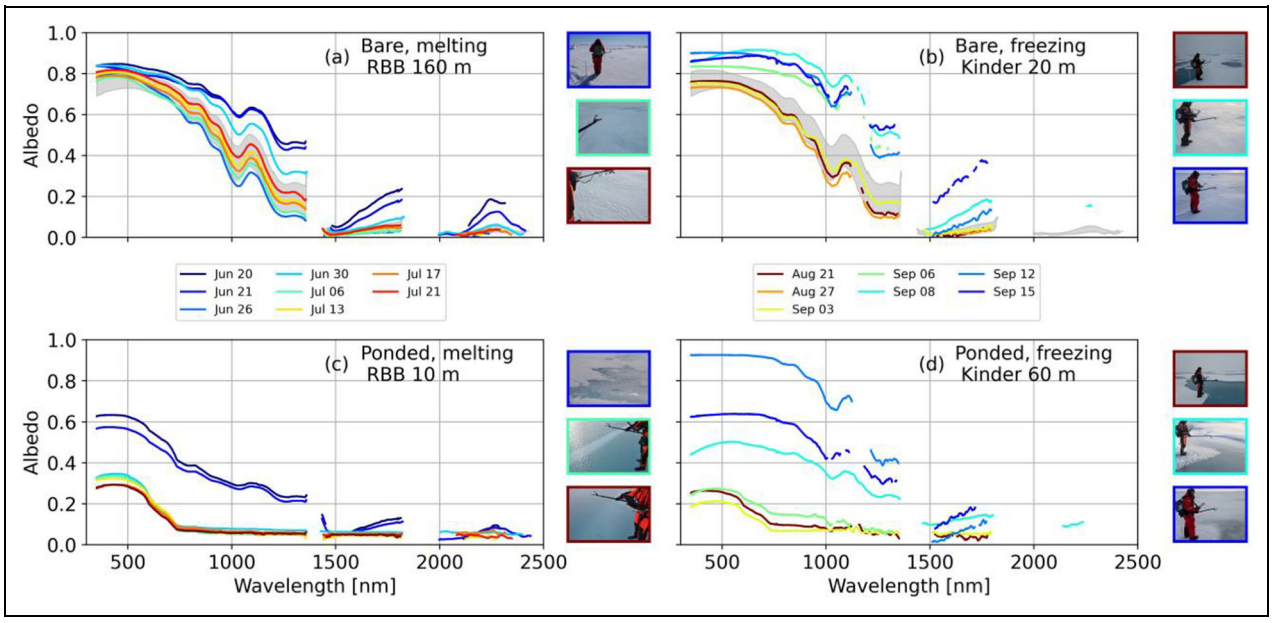

Figure 10. Spectral albedo for illustrative bare and ponded locations during melt and freeze. Progression of bare ice during (a) melt (RBB line, 160 m) and (b) freeze up (Kinder line, 20 m), and of ponded ice during (c) melt (RBB line, 10 m) and (d) freeze up (Kinder line, 60 m). Each curve is color-coded for a different date at the designated position. Gray shading indicates the one standard deviation range for second-year ice albedo (teal curve in **Figure 3**). Photographs show measurement sites corresponding to color-coded frames for select albedos.

a single day during summer, showing α_λ evolution from pond formation (June 24; **Figure 9a**) to pond drainage (July 13; **Figure 9b**) and continued pond evolution (July 29; **Figure 9c**), and from pond evolution (August 21; **Figure 9d**) to the beginning of fall freeze up (September 5; **Figure 9e**) and advanced freeze up (September 10; **Figure 9f**). There is a general decrease in albedo at all wavelengths as the melt season progresses (comparing June 24 and July 29, **Figure 9a** and **c**). In particular, α_λ at visible wavelengths (400–700 nm) decreases as the remnant snow cover melts (i.e., at 130 m) and melt ponds form (i.e., at approximately 15 and 30 m). Despite the overall trend in decreasing α_λ, an increase in α_λ is notable at visible wavelengths between 90 and 120 m from June 24 to July 13 (**Figure 9a** and **b**). This increase occurred as the result of a pond drainage event between July 11 and 13 (see Webster et al., 2022) that reduced the areal coverage of ponded ice. Subsequent increases in the depth and extent of ponds along with the decreased thickness of pond floors between July 13 and 29 resulted in an overall decrease in spectral albedo, which was most notable at visible wavelengths. The overall progression during melt resulted in increased spatial heterogeneity, which is particularly evident by comparing the spatial frequency of α_λ at visible wavelengths between June 24 and August 21. Due to the large absorption of near-infrared light by both water and ice, the albedos at wavelengths longer than 1,000 nm show reduced variability between bare and ponded ice.

Illustration of the temporal evolution of α_λ during freeze up (**Figure 9d–f**) shows that the ice surface was still melting on August 21 and pond coverage was 35–48% (compared with the peak value of 41% observed in July on the LD line at CO2). By September 5, freeze up had begun and some ponds had grown lids, increasing albedo at all wavelengths, but particularly pronounced at near-infrared wavelengths. For example, $a_{500\ nm}$ increased from 0.65 on August 21 to 0.85 September 5 at the 45 m point along the Kinder line (**Figure 9d** and **e**). Over the same time interval, the increase at 1,000 nm was from 0.32 to 0.73. On September 10, surface freeze up was complete along the line except for a pond at 10 m. Where the surface was frozen, new snow accumulated and α_λ values representative of snow-covered ice became prevalent. While some spatial variability in α_λ remained (as the snow was not yet uniformly optically thick), this progression illustrates how the large spatial variability of the summer ice cover is erased during fall freeze up.

The overall albedo evolution through melt and freeze up was dominated by the temporal changes in both bare and ponded ice types, as illustrated in **Figure 10** for select locations and days during Legs 4 and 5 on the RBB and Kinder survey lines. For melting, non-ponded ice sampled on RBB (160 m), melting snow (0.09 m thickness) was noted at the surface on June 20 and 21, and α_λ was correspondingly high (**Figure 10a**). When the site was next measured on June 26, α_λ was substantially lower at all wavelengths and the surface had 0.02 m of loose, granular material and a porous character. Whether these grains were originally snow or sea ice is unknown, but the lower α_λ for this date is consistent with the thinner layer. The June 30 α_λ showed significant rebound, consistent with observed increased surface layer thickness of 0.05 m. This sequence of measurements suggests an evolution from melting snow to a nascent and then deepening SSL. In this case, a slow, steady decrease in α_λ was not observed.

The SSL thickness stabilized at 0.04–0.05 m thickness for the remainder of CO2, and the observed α_λ values sampled beginning July 6 appeared to be consistent with the average α_λ for bare, melting ice (gray shading in **Figure 10a** and **b**).

During freeze up for bare ice sampled on the Kinder Line (20 m; **Figure 10b**), the observed α_λ transitioned with the freezing of liquid water in the surface layers (September 3), the accumulation of light snow (6, 8, 12 Sept), and then a rain-on-snow event (September 13–14, not shown). The α_λ on September 15 shows a notable increase in the wavelength band of 1,500–1,800 nm, suggesting enhanced scattering at the surface, possibly where liquid water that fell on the snow during the recent storm had refrozen, forming highly scattering ice crystals on the surface. Because of the SSL, the albedo evolution for bare ice experienced during freeze up is not simply a reverse of the melt evolution. During melt, the SSL develops. During freeze up, α_λ shows little change until snow accumulates.

Figure 10c shows the evolution of α_λ for a single pond on the RBB line (10 m) as melt progressed. Initially (June 20 and 21), the pond was shallow (0.025 m), but had refrozen, thus showing relatively high albedo. When measured on June 30, the pond surface was liquid, its depth had increased to 0.25 m, and the albedo dropped accordingly. As of the July 13 measurement, the pond depth had decreased to 0.10 m following the widespread pond drainage activity noted across the CO2 (see Webster et al., 2022). During this event, α_λ changed little despite the significant loss of water, which suggests that the optical properties of the pond floor remained relatively constant despite the drainage. As ponded ice maintains no SSL, the albedo of a pond during melt will only decrease; there is no mechanism for increasing the albedo of an open pond, until the pond begins to freeze and an ice lid forms.

Figure 10d shows the evolution of α_λ during freeze up for a pond on the Kinder line (60 m). The pond was initially liquid, with a depth of 0.34 m and low albedo (similar to the end-of-summer pond shown in **Figure 10c**). The time series shows the surface of the pond gradually freezing (September 8), accumulating snow (September 12), and the effects of rain-on-snow (September 15). Even though the albedo of this pond increased as it froze and accumulated snow, with albedo even higher than for the freezing bare ice on September 12, its albedo appears to be impacted by the rain event more strongly than the bare ice, suggesting that the albedo was still sensitive to the history of ponding.

As with bare, melting ice, the melt and freeze evolutions of ponded ice appear to show considerable asymmetry. This asymmetry is evident in the freeze up of the ponded ice (**Figure 10d**), where the formation of ice lids on ponds as well as rain-on-snow events significantly alter the albedo in ways not seen in initial pond formation. These observations suggest that some albedo transitions, particularly during the freeze up season, are abrupt and may be event-driven by phenomena such as rapid fluctuations in temperature around the freezing point or a snow or rain event. Such events contrast with processes that happen more gradually, such as snow ablation, pond deepening, and steady snow accumulation.

3.2.4. Temporal evolution of areal average albedo and comparison with SHEBA

Figure 11 presents a time series of α_{tot} averaged for all points along each of three survey lines (CO1, CO2, CO3) at MOSAiC and SHEBA. The three MOSAiC survey lines include ROV3 (Leg 3 CO1), LD (Leg 4 CO2), and Kinder (Leg 5 CO3). These three lines had the most comprehensive temporal and spatial records for each leg. All points on this figure represent clean ice as they do not include locations with appreciable sediment content. Both time series show consistent features: the presence of a seasonal snow cover until late May; an albedo reduction resulting from snow melt and melt pond formation during June; the gradual decline in albedo as ponds formed, grew, and deepened during July; an albedo increase resulting from the onset of freezing conditions in mid-August; the freezing of ponds; and the accumulation of snow in September. This progression is summarized by the five phases outlined by Perovich et al. (2002): dry snow, melting snow, pond formation, pond development, and freeze up.

The standard deviations of these two time series (dashed lines in **Figure 11**) are also strikingly similar. The spatial variability was low during the dry snow period (April–May), increased rapidly in June when the snow melted and ponds formed, and continued to increase throughout the pond evolution phase, reaching its peak just before the onset of sustained freezing conditions. The variability in optical properties during the summer continued to increase with time, likely due to the decreasing albedo of ponds, while the variability in pond size distribution decreased (Webster et al., 2022).

The apparent repeatability of the magnitude and variability in these two annual surveys from very different locations (high latitude Atlantic sector compared with Beaufort Sea; **Figure 1**) separated by 22 years is likely a result of elements of fundamental invariance in the evolution of the optical properties of Arctic sea ice. The albedos of accumulated snow and thick, bare, melting ice (**Figure 3**) are remarkably constant. The persistence of an SSL appears to buffer the albedo of thick, bare, melting sea ice such that it has surprisingly little sensitivity to either bottom or surface ablation, ice surface properties driven by radiative forcing, or synoptic weather events.

Despite the stability of α_{tot} for bare ice, differences in the areal coverage of melt ponds and the highly variable α_{tot} of ponded ice (**Figure 5**) could be expected to drive significant differences in the seasonal progression of the area average α_{tot}. Areal pond fraction along the LD line at MOSAiC increased during the pond evolution phase to a peak value of 41% at the end of July (Webster et al., 2022). Similarly, the near-maximum pond coverage for the larger MOSAiC area was 22%. In comparison, the pond fraction along the SHEBA albedo line increased to 38%, although aerial surveys suggest that a peak value close to 24% was more representative of the larger SHEBA region (Perovich et al., 2002). While the finding that the regions

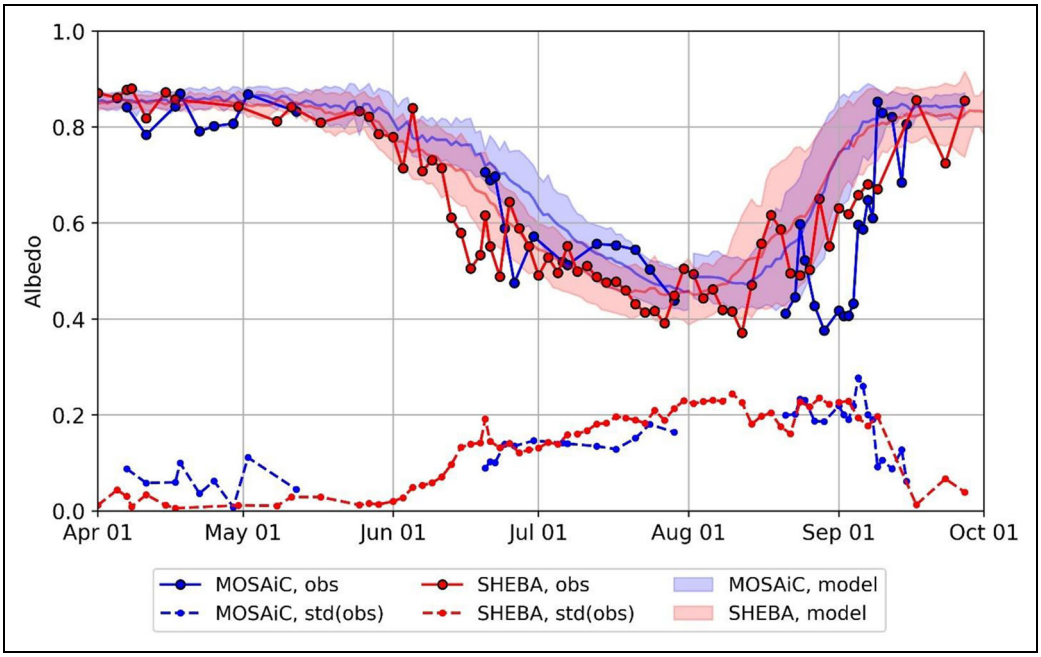

Figure 11. Seasonal evolution of average total albedo from April 1 to September 30. Average total albedo for MOSAiC (blue) and SHEBA (red; Perovich et al., 2002) campaigns, where MOSAiC values are averaged over the length of survey lines ROV3 (April–May), LD (June–July), and Kinder (August–September). The standard deviation (std) of measured (observed, obs) albedos is shown with dashed lines (for MOSAiC n = 14, 41, 29 for ROV3, LD, and Kinder survey lines, respectively; for SHEBA, n = 80). Background lines and shading show CESM2 predicted grid cell average albedo at points representing MOSAiC (blue, where two grid cells were employed: April–July on CO1/CO2 at 82.089 N°, 8.006 E°; August–September on CO3 at 88.197 N°, 103.908 E°) and SHEBA (red, single grid cell centered on 77.352 N°, 193.008 E°) from five ensemble members over five years (2015–2019) with standard deviation shown as shaded region. Grid cell center coordinates are indicated with stars in **Figure 1**. Note discontinuity in model ensemble average and shading at August 1 when model grid cell was moved from representing CO1/CO2 to CO3.

around these two field programs experienced very similar pond coverage (22% and 24%) may be coincidental, it nonetheless reinforces the repeatability of the areal average α_{tot} time series.

The impact of melt pond albedos on the variability of areal averaged albedo is, however, somewhat smaller than might be expected for at least two reasons. First, the variability in α_λ for ponds is strong only at visible wavelengths. The variability decreases at wavelengths beyond the visible spectrum, where the reflected component is dominated by the significant absorption incurred by the pond water where negligible scattering exists (**Figure 5**). Because roughly 30–50% of the energy in incident solar radiation reaching the ice surface is from wavelengths longer than those of visible light (700 nm), ponded areas generally absorb one third to one half of the incident sunlight, regardless of whether the area is dominated by light (high albedo) or dark (low albedo) ponds. Second, the ponds observed in these field studies occupied only a fraction of the surface, so the variability they introduce is scaled by this coverage.

Another feature common to the two albedo time series is a minimum average α_{tot} of 0.37. This low point was recorded on August 12 at SHEBA and on August 29 at MOSAiC (Leg 5). An even lower α_{tot} possibly could have been recorded between July 29 and August 29 on Leg 4 had the CO2 floe remained intact. Neither time series shown in **Figure 11** included significant contributions from sediment-laden ice, which would have further reduced the magnitude of this minimum albedo. Studies using a one-dimensional sea ice thermodynamic model (Maykut and Untersteiner, 1971) suggest that an albedo of 0.45 results in the rapid demise of an ice cover. The observational results presented here confirm that large-area average albedo for an intact ice cover can be this low or lower during July. Clearly, more details about the radiative and mass budgets, dynamic properties, and three-dimensional characteristics of an ice cover are needed to understand the implications of sustained low albedo on ice cover longevity.

4. Simulating the albedo of the sea ice cover in climate models

A range of frameworks exists for numerical simulation of the shortwave radiation budgets of the sea ice cover. Empirical frameworks parameterize albedo as a function of state variables describing the physical condition of the ice. Physical frameworks compute the albedo of the ice cover by simulating the spatial coverage of various surface types paired with information about the optical properties for each type. The merits and challenges of both approaches are discussed here.

4.1. Empirical models

An empirical framework was successfully applied by Perovich et al. (2011; 2020), where the seasonal time series of aggregate-scale albedo recorded at SHEBA (red curve in **Figure 11**) was stretched and compressed, respectively, to fit melt and freeze onset dates. In this case, the line-averaged α_{tot} was taken to be comparable to modeled grid-cell average α_{tot}, which includes a variety of ice thicknesses and (seasonally dependent) surface types simultaneously. The similarity of the MOSAiC record of α_{tot} with the SHEBA record (as illustrated in **Figure 11**) suggests that this approach may be more broadly applicable for grid cells across the Arctic basin over time than previously assumed. Factors that could alter the pacing of this seasonal progression, other than the timing of melt and freeze onset, include the duration of the snow-melt phase, accumulated snow depth, amount and timing of new snow fall, synoptic weather events that alter surface optical properties, such as rain, and changes in incident solar radiation caused by changes in cloud cover.

4.2. Physical models

Advanced physical surface albedo models explicitly quantify the areal coverage of individual ice types and assess radiative partitioning based on this coverage and the optical properties of the various surface types. For example, CESM computes partitioning for three distinct "radiatively active" surface types: snow-covered ice, bare ice, and ponded ice (Holland et al., 2012). Albedos for individual ice types are computed from an inherent optical property database used in conjunction with a radiative transfer calculation. The fidelity of the aggregate albedo rests on accurate representation of the spatial coverage of each surface type in the simulated climate and accurate optical property characterization. But two "wrongs" can produce a compensating "right." For example, if pond coverage is overestimated and pond albedo is also overestimated, then arriving at an accurate estimate for the total radiative partitioning is possible. A flawed solution such as this one could cascade to other inaccuracies, such as (in this example) poorly estimated meltwater budgets. Correspondingly, the "wrongs" may not compensate in a future climate state, leading to inaccurate predictions.

In addition to observed α_{tot}, **Figure 11** shows CESM2-simulated aggregate albedo over the annual cycle for five ensemble members averaged over 2015–2019 in which tuning has been applied to improve the Arctic sea ice state (Kay et al., 2022). The simulated albedo progressions for the MOSAiC and SHEBA locations show good general agreement with the observed progressions. However, some differences could be indicative of specific physical processes in need of improved treatment in the model, such as the timing of the onset of both melt and freeze. Model runs appear to show delayed melt onset and accelerated freeze up, suggesting that CESM2 predicts a shorter melt pond season than observed, consistent with comparisons between observed and predicted pond coverage (see Webster et al., 2022). The transition intervals associated with melt and freeze onset are accompanied by substantial physical changes occurring within the ice cover, such as rapid snow melt, initial pond formation, pond lid formation, and snow accumulation. Also, the 0.37 minimum albedo observed in both field records was more than one standard deviation below the model mean. This difference could be tied to differences in freeze onset timing between observations and the model predictions, suggestive of an Arctic ice cover with ponds that may have larger volume or higher salinity than simulated, resulting in longer response time to freezing conditions.

Both the observed and simulated melt at MOSAiC lag behind SHEBA by about two weeks. While the latitudinal difference is substantial (SHEBA simulation centered on 77 N°, MOSAiC CO1/CO2 on 82 N°), the initial melt onset at both locations occurred within a few calendar days. Beyond the onset timing, other factors that may impact this comparison include synoptic weather events and the summer-time northward drift of SHEBA and southward drift of MOSAiC. Significant variability also exists in the observed albedo time series, but whether the frequency and magnitude of this variability is needed for accurate simulation of the defining elements of the seasonal albedo progression or whether the average is sufficient is unclear.

Ultimately, physical models are only as good as the optical property simulations of individual surface types upon which they rely. To parse the differences between observations and the model, we next considered an evaluation of optical properties for each surface type.

4.2.1. Optical properties of individual surface types

Because physical models rely on knowledge of the optical properties of the individual surface types, we examined the sub-grid scale distribution of albedo for each of the three surface types: bare, snow-covered, and ponded ice. To enable this evaluation of radiative partitioning, a subset of years from a CESM2 ensemble member was re-run with additional sub-grid surface output. Simulated albedos for each of the three surface types and each of the five ice thickness categories were captured daily over six years (2015–2020). In this analysis we considered only output in the MOSAiC CO2 grid cell during the month of July. **Figure 12** shows box and whisker plots for the simulated albedo for each surface type, as well as the full range of observed α_{tot} values recorded during the MOSAiC summer (see inset legend in **Figure 2**). Median and interval range values for the observations are not depicted to avoid making unrealistic comparisons, as the model values represent the full area in a grid cell, but the observations pertain only to a single survey line. Additionally, the albedo range for snow-covered ice was taken from observations for melting snow ($\alpha_{tot} = 0.6–0.8$) made during June. No measurement made in July had a field of view that was uniquely melting snow; all fields of view were mixed, either with bare or ponded ice. In each case, modeled daily results from the thinnest ice thickness category were omitted, consistent with the inherent observational sampling bias against thin ice. The model appears to capture the range of observed albedo for summer snow-covered ice and bare ice types. The simulated albedos for ponded ice, however, appear to be drastic overestimates, as almost

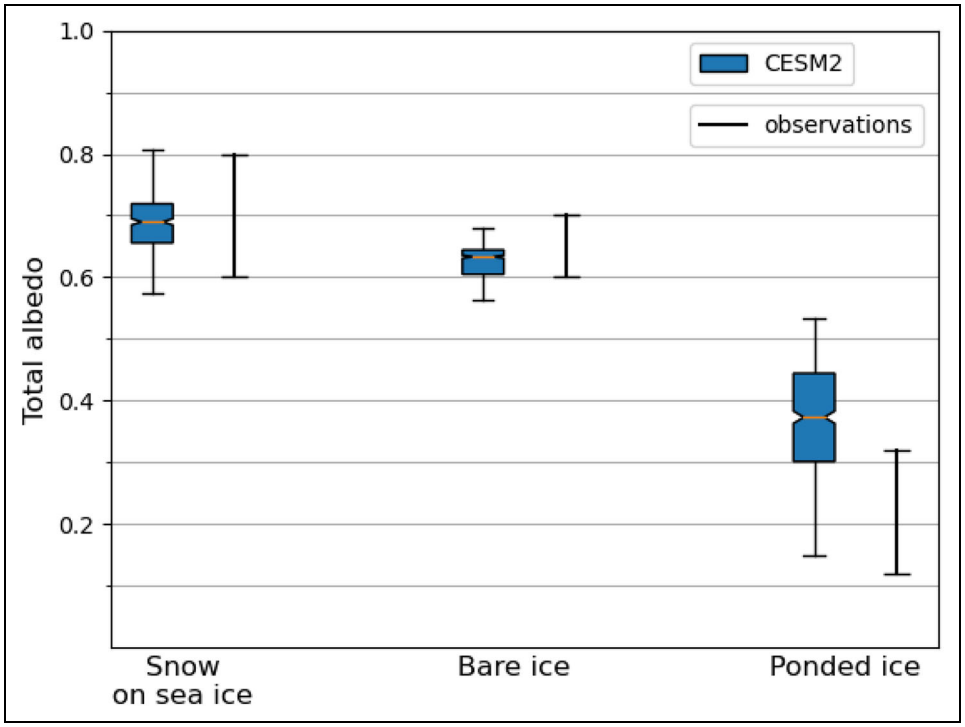

Figure 12. Distribution of modeled and range of observed individual surface type albedos. CESM2 modeled albedos for individual surface types (snow on sea ice, bare ice, ponded ice) during July for the MOSAiC-location grid cell (CO1/CO2; centered on 82.088°N, 8.006°E). Orange lines indicate median, blue boxes indicate range of values above the lowest 25% and below the highest 75% of all values; whiskers indicate ± 1.5 · interquartile range. Range of observed surface-specific albedos in July indicated by adjacent whiskers for approximately homogeneous fields of view measured at MOSAiC (see inset legend in **Figure 2**).

75% of simulated pond albedos in CESM2 during July have α_{tot} value higher than the full range of values observed at MOSAiC during July.

4.2.2. Albedo sensitivity to ice thickness

The area-averaged ice cover albedo typical of the summer melt season displays little sensitivity to time or place in large part because of the prevalence of thick, bare, melting sea ice with notably constant albedo (**Figure 3**). This ice has near-constant albedo because its highly scattering surface layer precludes albedo sensitivity to total ice thicknesses greater than 0.5–1 m. While there is large uncertainty about the physical characteristics of a reduced-ice Arctic in the coming decades, anticipated reductions in ice thickness may introduce albedo sensitivities to ice thickness for bare, melting ice. In particular, thinner ice with smaller freeboard would be expected to support SSLs with reduced physical and optical thickness. The thin ice case (teal curve in **Figure 2**) had an estimated total ice thickness of 0.4 m with 0.05-m thick SSL. Surface layers on thin sea ice with small freeboard would be expected to experience reduced backscattering due to flooding or wicking of liquid water. Additionally, while some thinner ice may maintain a robust SSL, overall thinning is anticipated to promote increased light transmittance to the ocean. Thinner ice is expected to also promote thinner pond floors, resulting in profound reductions in α_{λ} for ponded ice at visible wavelengths.

5. Summary and conclusions

Spectral and broadband albedos of the Arctic sea ice cover were documented by surface observers during the sunlit portion of the MOSAiC drift. Albedos were sampled manually along survey lines during the spring, throughout summer melt, and during autumn freeze up. Specific locations on various lines were identified as representative of individual ice surface types, including: melting snow cover in early summer; bare, thick melting ice, ponded ice, sediment laden ice and thinning ice during summer; and freezing melt ponds and snow-covered sea ice in autumn.

The time series documented at MOSAiC covered the established albedo progression of snow-covered, melting snow, pond formation, pond evolution, and freeze up (Perovich et al., 2002), although two logistics gaps precluded an uninterrupted time series on the same floe with continuous drift. Through comparison with the time series collected during SHEBA (1998), we suggest that the temporal progression of total albedo through the entire sunlit season has elements that remain invariant with respect to location, decade, and age of the ice cover.

The MOSAiC record was used to investigate specific elements indicative of the temporal variability of this record. The α_{λ} and α_{tot} (0.64 ± 0.04) of thick, bare, melting sea ice have small spatial and temporal variability. While such invariability has been attributed to the persistence of SSLs on bare, melting sea ice during the summer melt season (Perovich et al., 2002), we suggest that the optical

properties of this thin layer are remarkably consistent across first-year, second-year, and multiyear ice types, such that the albedo of bare, melting sea ice is independent of ice age. This highly scattering layer is resilient and renewable, and appears to buffer effects of variations in the thickness and optical properties of the ice beneath, including the presence of absorbing constituents such as sediment.

Strong transitions were observed during the onset intervals of both melt and freeze. These intervals resulted in rapid changes in surface type and characteristic albedo. Specifically, the formation and development of melt ponds from their earliest "subnivean" stage (Webster et al., 2022) to mature ponding show large variability at visible wavelengths, making representative optical signatures for ponded ice difficult to identify. The shoaling and accumulation of sediment inclusions within melting sea ice also produce strong time-varying changes in albedo (**Figure 4**).

Portions of the RBB line (on CO2) contained significant amounts of sediment laden ice and had correspondingly reduced albedo during summer (**Figures 5** and **6**). What fraction of the larger region was affected by sediment is not known. Clearly, our estimates of the seasonal albedo progression should account for any contribution from ice with lower albedo. If future increases in ice production in the shelf regions of the Arctic entrain increasing amounts of sediment, then albedos during the snow-free portion of the evolution (July–August) may be reduced significantly. The presence of sediment inclusions likely also affects the mass budget of the ice cover, but this potential effect remains an open question.

Furthermore, a future Arctic with widespread reduced ice thickness could have strong implications for the albedo of the summer ice cover. **Figure 2** indicates a reduced α_λ for bare, melting sea ice with thickness 0.40 m. Presumably, the reduction in total ice thickness is somewhat mitigated by the presence of an SSL. These SSLs, however, have a nuanced dependence on ice thickness. As bare, melting ice thins, and freeboard decreases, SSLs are expected to become prone to flooding and reduced optical thickness, diminishing their ability to maintain a high albedo on such ice. This thin ice scenario is distinct from the case of ice formed in winter or spring that is thin because it is young and has not yet been exposed to enough sunlight to have formed a fully developed SSL. Additionally, a thinner ice cover is expected to have pond floors with reduced optical thickness, decreasing α_λ values for ponded ice even further. Physical models are clearly needed to predict albedo under conditions with diminishing ice thickness, especially around the periphery of the Arctic earlier in the melt season, where thin ice is already a prevalent surface type.

Improvements in physical modeling are needed to accurately simulate a variety of conditions now prevalent on the Arctic sea ice cover. Specifically, improved representations of melt pond optical properties are needed. The exaggerated melt pond coverage identified in CESM2 by Webster et al. (2022), for example, may be compensated by the unrealistically high melt pond albedo seen in **Figure 12**, providing a possible case of two "wrongs" compensating to achieve an apparent "right." To accurately simulate the response of the ice cover to both synoptic time-scale weather events and long-term climatic change, more detailed characterizations are also needed to describe the optical effects of entrained sediment, rain, and decreasing ice thickness. These data are informing ongoing efforts to develop, validate, and improve the numerical simulation of the surface radiative and mass budgets of the Arctic ice cover. The wealth of α_λ data from MOSAiC will be central to these improvements.

Data accessibility statement

- MOSAiC albedo data are published at the National Science Foundation's Arctic Data Center as three separate datasets.
- **Smith, M, Light, B, Perovich, D, Webster, M, Anhaus, P, Clemens-Sewall, D, Linhardt, F, Macfarlane, A, Raphael, I, Bozzato, D, Brasseur, Z, Dadic, R, Fons, S, Immerz, A, Hannula, H, Hutchings, J, Pätzold, F, Regnery, J, Pirazzini, R, Tavri, A.** 2021. Broadband albedo measurements of the sea ice surface during the Multidisciplinary drifting Observatory for the Study of Arctic Climate (MOSAiC) campaign in the Central Arctic Ocean, April–September, 2020. doi:10.18739/A2KK94D36.
- **Smith, M, Light, B, Perovich, D, Webster, M, Anhaus, P, Clemens-Sewall, D, Linhardt, F, Macfarlane, A, Raphael, I, Bozzato, D, Brasseur, Z, Dadic, R, Fons, S, Immerz, A, Hannula, H, Hutchings, J, Pätzold, F, Regnery, J, Pirazzini, R, Tavri, A.** 2021. Spectral albedo measurements of the sea ice surface during the Multidisciplinary drifting Observatory for the Study of Arctic Climate (MOSAiC) campaign in the Central Arctic Ocean, April–September 2020. Arctic Data Center. doi:10.18739/A2FT8DK8Z.
- **Smith, M, Light, B, Perovich, D, Webster, M, Anhaus, P, Clemens-Sewall, D, Linhardt, F, Macfarlane, A, Raphael, I, Bozzato, D, Brasseur, Z, Dadic, R, Fons, S, Immerz, A, Hannula, H, Hutchings, J, Pätzold, F, Regnery, J, Pirazzini, R, Tavri, A.** 2021. Photos of the sea ice surface corresponding to surface albedo datasets collected during the Multidisciplinary drifting Observatory for the Study of Arctic Climate (MOSAiC) campaign in the Central Arctic Ocean, April–September 2020. Arctic Data Center. doi:10.18739/A2B27PS3 N. Albedo data from the SHEBA field campaign are available in Perovich et al. (2002).
- Albedo data from the ICESCAPE field campaign are available in Light et al. (2015).
- The tuned model runs from CESM2 are available via Globus access to NCAR GLADE at: /glade/campaign/cgd/ppc/cesm2_tuned_albedo. For more information on using Globus on NCAR systems, please refer to https://www2.cisl.ucar.edu/resources/storage-and-file-systems/globus-file-transfers.

Supplemental files

The supplemental files for this article can be found as follows:

Figure S1. Docx

Acknowledgments

Data used in this manuscript were produced as part of the international Multidisciplinary drifting Observatory for the Study of the Arctic Climate (MOSAiC) with the tag MOSAiC20192020 and the Project_ID: AWI_PS122_00. Meteorological measurements associated with the Surface Meteorological Instrumentation (PWD) and Aerosol Observing System (AOSMET) from the Atmospheric Radiation Measurement (ARM) User Facility, a U.S. Department of Energy (DOE) Office of Science User Facility managed by the Biological and Environmental Research Program, April 1, 2020 to September 30, 2020, ARM Mobile Facility (MOS) MOSAIC (Drifting Obs–Study of Arctic Climate), AMF2 (M1), as compiled by J. Kyrouac, S. Springston, and D. Holdridge, ARM Data Center, accessed May 27, 2021, at http://dx.doi.org/10.5439/1025153. We thank all people involved in the expedition of the research vessel *Polarstern* during MOSAiC in 2019–2020, as listed in Nixdorf et al. (2021). For the CESM simulations, we acknowledge computing and data storage resources, including the Cheyenne supercomputer (doi:10.5065/D6RX99HX), which were provided by the Computational and Information Systems Laboratory (CISL) at NCAR. NCAR is sponsored by the National Science Foundation. We thank Steven Fons, Hannula Henna-Reetta, Jennifer Hutchings, Falk Pätzold, Roberta Pirazzini, and Julia Regnery for their capable assistance in the field. We appreciate the efforts of the editorial staff at *Elementa* and two anonymous reviewers who helped improved the manuscript.

Funding

BL conducted this work under the U.S. National Science Foundation grant OPP-1724467. MMS was supported by NSF OPP-1724467 and OPP-1724748. DKP, DC-S, and IAR conducted this work under NSF OPP-1724540. MAW conducted this work under the National Aeronautics and Space Administration's New Investigator Program in Earth Science (80NSSC20K0658). MMH and DB acknowledge funding from NSF OPP-1724748. FL was supported by the BMWi project ArcticSense (50EE1917A) and by Prof. Dr. Werner Petersen-Stiftung. ARM acknowledges funding from DEARice and the Swiss Polar Institute. PA was funded through the Alfred-Wegner-Institutes internal project AWI_ROV and additional funds through the German Ministry of Education and Research (BMBF) project DiatomARCTIC (03F0810A).

Competing interests

The authors declare that they have no competing interests.

Author contributions

Contributed to the conception and design: BL, DKP, MMH, MMS.

Contributed to the acquisition of data: MMS, MAW, FL, IR, DC-S, ARM, PA.

Contributed to analysis and interpretation of data: BL, MMS, DKP, MAW, MMH, DB.

Drafted and/or revised the article: All authors.

Approved the submitted version for publication: All authors.

References

Alfred Wegener Institute (AWI). 2017. Polar research and supply vessel *Polarstern* operated by the Alfred Wegener Institute Helmholtz Centre for polar and marine research. *Journal of Large-scale Research Facilities* **3**: A119. DOI: https://doi.org/10.17815/jlsrf-3-163.

Aoki, T, **Kuchiki, K**, **Niwano, M**, **Kodama, Y**, **Hosaka, M**, **Tanaka, T.** 2011. Physically based snow albedo model for calculating broadband albedos and the solar heating profile in snowpack for general circulation models. *Journal of Geophysical Research* **116**: D11114. DOI: https://doi.org/10.1029/2010JD015507.

Arrigo, KR. 2015. Impacts of Climate on EcoSystems and Chemistry of the Arctic Pacific Environment (ICESCAPE). *Deep Sea Research Part II: Topical Studies in Oceanography* **118**: 1–6. DOI: https://doi.org/10.1016/j.dsr2.2015.06.007.

Brandt, RE, **Warren, SG**, **Worby, AP**, **Grenfell, TC.** 2005. Surface albedo of the Antarctic sea ice zone. *Journal of Climate* **18**(17): 3606–3622. DOI: https://doi.org/10.1175/JCLI3489.1

Briegleb, BP, **Light, B.** 2007. A delta-eddington mutiple scattering parameterization for solar radiation in the sea ice component of the community climate system model (No. NCAR/TN-472+STR). Boulder, CO: University Corporation for Atmospheric Research. DOI: https://doi.org/10.5065/D6B27S71.

Cavalieri, DJ, **Parkinson, CL**, **Gloersen, P**, **Zwally, HJ.** 1996. *Sea ice concentrations from nimbus-7 SMMR and DMSP SSM/I-SSMIS passive microwave data, version 1.* Boulder, CO: NASA National Snow and Ice Data Center Distributed Active Archive Center. DOI: https://doi.org/10.5067/8GQ8LZQVL0VL.

Danabasoglu, G, **Lamarque, JF**, **Bachmeister, J**, **Bailey, DA**, **DuVivier, AK**, **Edwards, J**, **Emmons, LK**, **Fasullo, J**, **Garcia, R**, **Gettelman, A**, **Hannay, C**, **Holland, MM**, **Large, WG**, **Lauritzen, PH**, **Lawrence, DM**, **Lenaerts, JTM**, **Lindsay, K**, **Lipscomb, WH**, **Mills, MJ**, **Neale, R**, **Oleson, KW**, **Otto-Bliesner, B**, **Phillips, AS**, **Sacks, W**, **Tilmes, S**, **van Kampenhout, L**, **Vertenstein, M**, **Bertini, A**, **Dennis, J**, **Deser, C**, **Fischer, C**, **Fox-Kemper, B**, **Kay, JE**, **Kinnison, D**, **Kushner, PJ**, **Larson, VE**, **Long, MC**, **Mickelson, S**, **Moore, JK**, **Nienhouse, E**, **Polvani, L**, **Rasch, PJ**, **Strand, WG.** 2020. The community earth system model version 2 (CESM2). *Journal of Advances in Modeling Earth Systems* **12**. DOI: https://doi.org/10.1029/2019MS001916.

Divine, DV, **Granskog, MA**, **Hudson, SR**, **Pedersen, CA**, **Karlsen, TI**, **Divina, SA**, **Renner, AHH**, **Gerland, S.**

2015. Regional melt-pond fraction and albedo of thin Arctic first-year drift ice in late summer. *The Cryosphere* **9**(1): 255–268. DOI: https://doi.org/10.5194/tc-9-255-2015.

DuVivier, AK, **Holland, MM**, **Kay, JE**, **Tilmes, S**, **Gettelman, A**, **Bailey, DA.** 2020. Arctic and Antarctic sea ice state in the Community Earth System Model Version 2 and the influence of atmospheric chemistry. *Journal of Geophysical Research: Oceans* **125**(8). DOI: https://doi.org/10.1029/2019JC015934.

Ehn, J, **Granskog, MA**, **Papakyriakou, T**, **Galley, R**, **Barber, D.** 2006. Surface albedo observations of Hudson Bay (Canada) landfast sea ice during the spring melt. *Annals of Glaciology* **44**: 23–29. DOI: https://doi.org/10.3189/172756406781811376.

Eicken, H, **Lensu, M**, **Leppäranta, M**, **Tucker III, WB, Gow, AJ, Salmela, O.** 1995. Thickness, structure, and properties of level summer multiyear ice in the Eurasian sector of the Arctic Ocean. *Journal of Geophysical Research: Oceans* **100**(C11): 22697–22710.

Flanner, MG, **Zender, CS.** 2006. Linking snowpack microphysics and albedo evolution. *Journal of Geophysical Research* **111**(D12). DOI: https://doi.org/10.1029/2005JD006834.

Goldenson, N, **Doherty, SJ**, **Bitz, CM**, **Holland, MM**, **Light, B**, **Conley, AJ.** 2012. Arctic climate response to forcing from light-absorbing particles in snow and sea ice in CESM. *Atmospheric Chemistry and Physics* **12**(17): 7903–7920. DOI: https://doi.org/10.5194/acp-12-7903-2012.

Grenfell, TC. 1979. The effects of ice thickness on the exchange of solar radiation over the polar oceans. *Journal of Glaciology* **22**: 305–320.

Grenfell, TC, **Maykut, GA.** 1977. The optical properties of ice and snow in the Arctic Basin. *Journal of Glaciology* **18**(80): 445–463.

Grenfell, TC, **Perovich, DK.** 1984. Spectral albedos of sea ice and incident solar irradiance in the southern Beaufort Sea. *Journal of Geophysical Research Oceans* **89**(C3): 3573–3580.

Grenfell, TC, **Perovich, DK.** 2004. Seasonal and spatial evolution of albedo in a snow-ice-land-ocean environment. *Journal of Geophysical Research: Oceans* **109**(C1). DOI: https://doi.org/10.1029/2003JC001866.

Grenfell, TC, **Perovich, DK.** 2008. Incident spectral irradiance in the Arctic Basin during the summer and fall. *Journal of Geophysical Research* **113**(D12). DOI: https://doi.org/10.1029/2007JD009418.

Hall, A. 2004. The role of surface albedo feedback in climate. *Journal of Climate* **17**: 1550–1568.

Hanesiak, JM, **Barber, DG**, **De Abreu, RA**, **Yackel, JJ.** 2001. Local and regional albedo observations of Arctic first-year sea ice during melt ponding. *Journal of Geophysical Research* **106**: 1005–1016. DOI: https://doi.org/10.1029/1999JC000068.

Holland, MM, **Bailey, DA**, **Briegleb, BP**, **Light, B**, **Hunke, E.** 2012. Improved sea ice shortwave radiation physics in CCSM4: The impact of melt ponds and aerosols on arctic sea ice. *Journal of Climate* **25**: 1413–1430.

Holland, MM, **Landrum, L.** 2015. Factors affecting projected Arctic surface shortwave heating and albedo change in coupled climate models. *Philosophical Transactions of the Royal Society A: Mathematical, Physical and Engineering Sciences* **373**(2045): 20140162. DOI: https://doi.org/10.1098/rsta.2014.0162.

Hueni, A, **Bialek, A.** 2017. Cause, effect, and correction of field spectroradiometer interchannel radiometric steps. *IEEE Journal of Selected Topics in Applied Earth Observations and Remote Sensing* **10**(4): 1542–1551.

Hunkeler, PA. 2016. Sea-ice thickness and porosity from multi-frequency electromagnetic induction sounding: Application to the sub-ice platelet layer in Atka Bay, Antarctica [dissertation]. Bremen, Germany: Jacobs University. Available at https://epic.awi.de/id/eprint/40262/1/PHD_20160810_Hunkeler.pdf. Accessed September 2021.

Hunkeler, PA, **Hoppmann, M**, **Hendricks, S**, **Kalscheuer, T**, **Gerdes, R.** 2016. A glimpse beneath Antarctic sea ice: Platelet layer volume from multi-frequency electromagnetic induction sounding. *Geophysical Research Letters* **43**(1). DOI: https://doi.org/10.1002/2015gl065074.

Itkin, P, **Webster, M**, **Hendricks, S**, **Oggier, M**, **Jaggi, M**, **Ricker, R**, **Arndt, S**, **Divine, DV**, **von Albedyll, L**, **Raphael, I**, **Rohde, J**, **Liston, GE.** 2021. Magnaprobe snow and melt pond depth measurements from the 2019–2020 MOSAiC expedition. *PANGAEA*. Available at https://doi.pangaea.de/10.1594/PANGAEA.937781.

Katlein, C, **Arndt, S**, **Belter, HJ**, **Castellani, G**, **Nicolaus, M.** 2019. Seasonal evolution of light transmission distributions through Arctic sea ice. *Journal of Geophysical Research Oceans* **124**(8): 5418–5435.

Kay, JE, **DeRepentigny, P**, **Holland, MM**, **Bailey, DA**, **DuVivier, AK**, **Blanchard-Wrigglesworth, E**, **Deser, C**, **Jahn, A**, **Singh, H**, **Smith, MM**, **Webster, MA**, **Edwards, J**, **Lee, SS**, **Rodgers, KB**, **Rosenbloom, NA.** 2022. Less surface sea ice melt in the CESM2 improves Arctic sea ice simulation with minimal non-polar climate impacts. *Journal of Advances in Modeling Earth Systems*. DOI: https://doi.org/10.1029/2021MS002679.

Keen, A, **Blockley, E**, **Bailey, DA**, **Boldingh Debernard, J**, **Bushuk, M**, **Delhaye, S**, **Docquier, D**, **Feltham, D**, **Massonnet, F**, **O'Farrell, S**, **Ponsoni, L**, **Rodriguez, JM**, **Schroeder, D**, **Swart, N**, **Toyoda, T**, **Tsujino, H**, **Vancoppenolle, M**, **Wyser, K.** 2021. An intercomparison of the mass budget of the Arctic sea ice in CMIP6 models. *The Cryosphere* **15**: 951–982. DOI: https://doi.org/10.5194/tc-15-951-2021.

Krumpen, T, **Birrien, F**, **Kauker, F**, **Rackow, T**, **von Albedyll, L**, **Angelopoulos, M**, **Belter, HJ**, **Bessonov, V**, **Damm, E**, **Dethloff, K**, **Haapala, J**, **Haas, C**, **Harris, C**, **Hendricks, S**, **Hoelemann, J**, **Hoppmann, M**, **Kaleschke, L**, **Karcher, M**, **Kolabutin, N**, **Lei, R**, **Lenz, J**, **Morgenstern, A**, **Nicolaus, M**, **Nixdorf, U**,

Petrovsky, T, **Rabe, B**, **Rabenstein, L**, **Rex, M**, **Ricker, R**, **Rohde, J**, **Shimanchuk, E**, **Singha, S**, **Smolyanitsky, V**, **Sokolov, V**, **Stanton, T**, **Timofeeva, A**, **Tsamados, M**, **Watkins, D.** 2020. The MOSAiC ice floe: sediment-laden survivor from the Siberian shelf. *The Cryosphere* **14**: 2173–2187. DOI: https://doi.org/10.5194/tc-14-2173-2020.

Langleben, MP. 1969. Albedo and degree of puddling of a melting cover of sea ice. *Journal of Glaciology* **8**(54): 407–412.

Langleben, MP. 1971. Albedo of melting sea ice in the southern Beaufort Sea. *Journal of Glaciology* **10**(58): 101–104.

Light, B, **Eicken, H**, **Maykut, GA**, **Grenfell, TC.** 1998. The effect of included particulates on the spectral albedo of sea ice. *Journal of Geophysical Research* **103**(C12): 27739–27752.

Light, B, **Grenfell, TC**, **Perovich, DK.** 2008. Transmission and absorption of solar radiation by Arctic sea ice during the melt season. *Journal of Geophysical Research* **113**: C03023. DOI: https://doi.org/10.1029/2006JC003977.

Light, B, **Maykut, GA**, **Grenfell, TC.** 2004. A temperature-dependent, structural-optical model of first-year sea ice. *Journal of Geophysical Research* **109**: C06013. DOI: https://doi.org/10.1029/2003JC002164.

Light, B, **Perovich, DK**, **Webster, MA**, **Polashenski, C**, **Dadic, R.** 2015. Optical properties of melting first-year Arctic sea ice. *Journal of Geophysical Research: Oceans* **120**(11). DOI: https://doi.org/10.1002/2015JC011163.

Maykut, GA, **Untersteiner, N.** 1971. Some results from a time-dependent thermodynamic model of sea ice. *Journal of Geophysical Research* **76**(6): 1550–1575. DOI: https://doi.org/10.1029/JC076i006p01550.

Mundy, CJ, **Ehn, JK**, **Barber, DG**, **Michel, C.** 2007. Influence of snow cover and algae on the spectral dependence of transmitted irradiance through Arctic landfast first-year sea ice. *Journal of Geophysical Research* **112**(C03). DOI: https://doi.org/10.1029/2006JC003683.

Nicolaus, M, **Gerland, S**, **Hudson, SR**, **Hanson, S**, **Haapala, J**, **Perovich, DK.** 2010. Seasonality of spectral albedo and transmittance as observed in the Arctic Transpolar Drift in 2007. *Journal of Geophysical Research* **115**(C11). DOI: https://doi.org/10.1029/2009JC006074.

Nicolaus, M, **Katlein, C**, **Maslanik, J**, **Hendricks, S.** 2012. Changes in Arctic sea ice result in increasing light transmittance and absorption. *Geophysical Research Letters* **39**: L24501.

Nicolaus, M, **Perovich, DK**, **Spreen, G, Granskog, MA**, **Albedyll, L**, **von Angelopoulos, M**, **Anhaus, P**, **Arndt, S**, **Belter, HJ**, **Bessonov, V**, **Birnbaum, G**, **Brauchle, J**, **Calmer, R**, **Cardellach, E**, **Cheng, B**, **Clemens-Sewall, D**, **Dadic, R**, **Damm, E**, **deBoer, G**, **Demir, O**, **Dethloff, K**, **Divine, DV**, **Fong, AA**, **Fons, S**, **Frey, MM**, **Fuchs, N**, **Gabarró, C**, **Gerland, S**, **Goessling, HF**, **Gradinger, R**, **Haapala, J**, **Haas, C**, **Hamilton, J**, **Hannula, H-R**, **Hendricks, S**, **Herber, A**, **Heuzé, C**, **Hoppmann, M**, **Høyland, KV**, **Huntemann, M**, **Hutchings, JK**, **Hwang, B**, **Itkin, P**, **Jacobi, H-W**, **Jaggi, M**, **Jutila, A**, **Kaleschke, L**, **Katlein, C**, **Kolabutin, N**, **Krampe, D**, **Kristensen, SS**, **Krumpen, T**, **Kurtz, N**, **Lampert, A**, **Lange, BA**, **Lei, R**, **Light, B**, **Linhardt, F**, **Liston, GE**, **Loose, B**, **Macfarlane, AR**, **Mahmud, M**, **Matero, IO**, **Maus, S**, **Morgenstern, A**, **Naderpour, R**, **Nandan, V**, **Niubom, A**, **Oggier, M**, **Oppelt, N**, **Pätzold, F**, **Perron, C**, **Petrovsky, T**, **Pirazzini, R**, **Polashenski, C**, **Rabe, B**, **Raphael, IA**, **Regnery, J**, **Rex, M**, **Ricker, R**, **Riemann-Campe, K**, **Rinke, A**, **Rohde, J**, **Salganik, E**, **Scharien, RK**, **Schiller, M**, **Schneebeli, M**, **Semmling, M**, **Shimanchuk, E**, **Shupe, MD**, **Smith, MM**, **Smolyanitsky, V**, **Sokolov, V**, **Stanton, T**, **Stroeve, J**, **Thielke, L**, **Timofeeva, A**, **Tonboe, RT**, **Tavri, A**, **Tsamados, M**, **Wagner, DN**, **Watkins, D**, **Webster, M**, **Wendisch M.** 2022. Overview of the MOSAiC expedition: Snow and sea ice. *Elementa: Science of the Anthropocene*. DOI: https://doi.org/10.1525/elementa.2021.000046vv.

Nixdorf, U, **Dethloff, K**, **Rex, M**, **Shupe, M**, **Sommerfeld, A**, **Perovich, DK**, **Nicolaus, M**, **Heuzé, C**, **Rabe, B**, **Loose, B**, **Damm, E**, **Gradinger, R**, **Fong, A**, **Maslowski, W**, **Rinke, A**, **Kwok, R**, **Spreen, G**, **Wendisch, M**, **Herber, A**, **Hirsekorn, M**, **Mohaupt, V**, **Frickenhaus, S**, **Immerz, A**, **Weiss-Tuider, K**, **König, B**, **Mengedoht, D**, **Regnery, J**, **Gerchow, P**, **Ransby, D**, **Krumpen, T**, **Morgenstern, A**, **Haas, C.** 2021. MOSAiC extended acknowledgement. *Zenodo*. DOI: https://doi.org/10.5281/zenodo.5179738.

Perovich, DK. 1991. Seasonal changes in sea ice optical properties during fall freeze-up. *Cold Regions Science and Technology* **19**(3): 261–273.

Perovich, DK. 1994. Light reflection from sea ice during the onset of melt. *Journal of Geophysical Research: Oceans* **99**(C2): 3351–3359.

Perovich, DK, **Grenfell, TC**. 1981. Laboratory studies of the optical properties of young sea ice. *Journal of Glaciology* **27**(96): 331–346.

Perovich, DK, **Grenfell, TC**, **Light, B**, **Hobbs, PV.** 2002. Seasonal evolution of the albedo of multiyear Arctic sea ice. *Journal of Geophysical Research* **107**(C10): 8044. DOI: https://doi.org/10.1029/2000JC000438.

Perovich, DK, **Jones, KF**, **Light, B**, **Eicken, H**, **Markus, T**, **Stroeve, J**, **Lindsay, R.** 2011. Solar partitioning in a changing Arctic sea-ice cover. *Annals of Glaciology* **52**: 192–196. DOI: https://doi.org/10.3189/172756411795931543.

Perovich, DK, **Light, B**, **Dickinson, S.** 2020. Changing ice and changing light: Trends in solar heat input to the upper Arctic Ocean from 1988 to 2014. *Annals of Glaciology*. DOI: https://doi.org/10.1017/aog.2020.62.

Perovich, DK, **Polashenski, C**. 2012. Albedo evolution of seasonal Arctic sea ice. *Geophysical Research Letters*

39: L08501. DOI: https://doi.org/10.1029/2012GL051432.

Perovich, DK, **Richter-Menge, JA**, **Tucker, WB.** 2001. Seasonal changes in Arctic sea-ice morphology. *Annals of Glaciology* **33**: 171–176.

Polashenski, C, **Golden, KM**, **Perovich, DK**, **Skyllingstad, E**, **Arnsten, A**, **Stwertka, C**, **Wright, N.** 2017. Percolation blockage: A process that enables melt pond formation on first year Arctic sea ice. *Journal of Geophysical Research: Oceans* **122**: 413–440. DOI: https://doi.org/10.1002/2016JC011994.

Polashenski, C, **Perovich, DK**, **Courville, Z.** 2012. The mechanisms of sea ice melt pond formation and evolution. *Journal of Geophysical Research* **117**(C01). DOI: https://doi.org/10.1029/2011JC007231.

Reimnitz, E. 1994. Sediments in sea ice. *Berichte zur Polarforschung* **149**: 69–73.

Schneebeli, M, **Johnson, JB.** 1998. A constant-speed penetrometer for high-resolution snow stratigraphy. *Annals of Glaciology* **26**: 107–111. DOI: https://doi.org/10.3189/1998AoG26-1-107-111.

Smith, M, **Light, B**, **Perovich, D**, **Webster, M**, **Anhaus, P**, **Clemens-Sewall, D**, **Linhardt, F**, **Macfarlane, A**, **Raphael, I**, **Bozzato, D**, **Brasseur, Z**, **Dadic, R**, **Fons, S**, **Immerz, A**, **Hannula, H**, **Hutchings, J**, **Pätzold, F**, **Regnery, J**, **Pirazzini, R**, **Tavri, A.** 2021a. Spectral albedo measurements of the sea ice surface during the MOSAiC campaign in the Central Arctic Ocean, April–September 2020 [dataset]. Arctic Data Center. DOI: https://doi.org/10.18739/A2FT8DK8Z.

Smith, M, **Light, B**, **Perovich, D**, **Webster, M**, **Anhaus, P**, **Clemens-Sewall, D**, **Linhardt, F**, **Macfarlane, A**, **Raphael, I**, **Bozzato, D**, **Brasseur, Z**, **Dadic, R**, **Fons, S**, **Immerz, A**, **Hannula, H**, **Hutchings, J**, **Pätzold, F**, **Regnery, J**, **Pirazzini, R**, **Tavri, A.** 2021b. Broadband albedo measurements of the sea ice surface during the MOSAiC campaign in the Central Arctic Ocean, April–September 2020 [dataset]. Arctic Data Center. DOI: https://doi.org/10.18739/A2KK94D36.

Smith, M, **Light, B**, **Perovich, D**, **Webster, M**, **Anhaus, P**, **Clemens-Sewall, D**, **Linhardt, F**, **Macfarlane, A**, **Raphael, I**, **Bozzato, D**, **Brasseur, Z**, **Dadic, R**, **Fons, S**, **Immerz, A**, **Hannula, H**, **Hutchings, J**, **Pätzold, F**, **Regnery, J**, **Pirazzini, R**, **Tavri, A.** 2021c. Photos of the sea ice surface corresponding to surface albedo datasets collected during the Multidisciplinary drifting Observatory for the Study of Arctic Climate (MOSAiC) campaign in the Central Arctic Ocean, April–September 2020 [dataset]. Arctic Data Center. DOI: https://doi.org/10.18739/A2B27PS3N.

Sturm, M, **Holmgren, J.** 2018. An automatic snow depth probe for field validation campaigns. *Water Resources Research* **54**: 9695–9701. DOI: https://doi.org/10.1029/2018WR023559.wi

Taskjelle, T, **Hudson, SR**, **Granskog, MA**, **Nicolaus, M**, **Lei, R**, **Gerland, S**, **Stamnes, JJ**, **Hamre, B.** 2016. Spectral albedo and transmittance of thin young Arctic sea ice. *Journal of Geophysical Research Oceans* **121**: 540–553. DOI: https://doi.org/10.1002/2015JC011254.

Thackeray, CW, **Hall, A**. 2019. An emergent constraint on future Arctic sea-ice albedo feedback. *Nature Climate Change* **9**: 972–978.

Tucker III, WB, **Gow, AJ**, **Meese, DA**, **Bosworth, HW**, **Reimnitz, E.** 1999. Physical characteristics of summer sea ice across the Arctic Ocean. *Journal of Geophysical Research Oceans* **104**(C1): 1489–1504.

Untersteiner, N. 1961. On the mass and heat budget of Arctic sea ice. *Archiv für Meteorologie, Geophysik und Bioklimatologie Serie A* **12**(2): 151–182.

Uttal, T, **Curry, JA**, **McPhee, MG**, **Perovich, DK**, **Moritz, RE**, **Maslanik, JA**, **Guest, PS**, **Stern, HL**, **Moore, JA**, **Turenne, R**, **Heiberg, A**, **Serreze, MC**, **Wylie, DP**, **Persson, OG**, **Paulson, CA**, **Halle, C**, **Morison, JH**, **Wheeler, PA**, **Makshtas, A**, **Welch, H**, **Shupe, MD**, **Intrieri, JM**, **Stamnes, K**, **Lindsey, RW**, **Pinkel, R**, **Pegau, WS**, **Stanton, TP**, **Grenfeld, TC.** 2002. Surface heat budget of the Arctic Ocean. *Bulletin of the American Meteorological Society* **83**(2): 255–275.

Webster, MA, Holland, MM, Wright, NC, Hendricks, S, Hutter, N, Itkin, P, Light, B, Linhardt, F, Perovich, DK, Raphael, IA, Smith, MM, von Albedyll, L, Zhang, J. 2022. Spatiotemporal evolution of melt ponds in the Arctic: MOSAiC observations and model results. *Elementa: Science of the Anthropocene* **10**. DOI: 10.1525/elementa.2021.000072.

Webster, MA, **Rigor, IG**, **Perovich, DK**, **Richter-Menge, JA**, **Polashenski, CM**, **Light, B.** 2015. Seasonal evolution of melt ponds on Arctic sea ice. *Journal of Geophysical Research: Oceans* **120**: 5968–5982. DOI: https://doi.org/10.1002/2015JC011030.

Wunderling, N, **Willeit, M**, **Donges, JF**, **Winkelmann, R.** 2020. Global warming due to loss of large ice masses and Arctic summer sea ice. *Nature Communications* **11**(1): 1–8. DOI: https://doi.org/10.1038/s41467-020-18934-3.

Xia, W, **Xie, H.**, **Ke, C**, **Zhao, J.**, **Lei, R**, **Ackley, SF.** 2015. Summer surface albedo of sea ice in Pacific Arctic sector as measured during the CHINARE 2010 cruise. *Arctic, Antarctic, and Alpine Research* **47**(4): 645–656. DOI: https://doi.org/10.1657/AAAR0014-090.

Zhu, J, **Liu, Y**, **Wang, X**, **Li, T.** 2021. Optical properties and surface energy flux of spring fast ice in the Arctic. *Acta Oceanologica Sinica* **40**(10): 84–96. DOI: https://doi.org/10.1007/s13131-021-1828-9.

Zubov, NN. 1979. Arctic ice (in Russian). Translated by U.S. Naval Oceanographic Office, 490. Moscow, Russia: Izdatel'stvo Glavsermorputi.

How to cite this article: Light, B, Smith, MM, Perovich, DK, Webster, MA, Holland, MM, Linhardt, F, Raphael, IA, Clemens-Sewall, D, Macfarlane, AR, Anhaus, P, Bailey, DA. 2022. Arctic sea ice albedo: Spectral composition, spatial heterogeneity, and temporal evolution observed during the MOSAiC drift. *Elementa: Science of the Anthropocene* 10(1). DOI: https://doi.org/10.1525/elementa.2021.000103

Domain Editor-in-Chief: Jody W. Deming, University of Washington, Seattle, WA, USA

Associate Editor: Stephen F. Ackley, Department of Geological Sciences, University of Texas at San Antonio, San Antonio, TX, USA

Knowledge Domain: Ocean Science

Part of an Elementa Special Feature: The Multidisciplinary Drifting Observatory for the Study of Arctic Climate (MOSAiC)

Published: August 4, 2022 **Accepted:** July 4, 2022 **Submitted:** November 7, 2021

ELEMENTA Science of the Anthropocene

Elem Sci Anth is a peer-reviewed open access journal published by University of California Press.

OPEN ACCESS